Icarus 204 (2009) 114–136

Contents lists available at ScienceDirect

Icarus

journal homepage: www.elsevier.com/locate/icarus

Water sorption on martian regolith analogs: Thermodynamics and near-infrared reflectance spectroscopy

Antoine Pommerol *, Bernard Schmitt, Pierre Beck, Olivier Brissaud

Laboratoire de Planétologie de Grenoble, Université J. Fourier, CNRS/INSU, Bât. D de Physique, B.P. 53, 38041 Grenoble Cedex 9, France

ARTICLE INFO

Article history:
Received 8 October 2008
Revised 6 June 2009
Accepted 16 June 2009
Available online 24 June 2009

Keywords:
Mars, surface
Spectroscopy
Mineralogy
Experimental techniques

ABSTRACT

The near-infrared reflectance spectra of the martian surface present strong absorption features attributed to hydration water present in the regolith. In order to characterize the relationships between this water and atmospheric vapor and decipher the physical state of water molecules in martian regolith analogs, we designed and built an experimental setup to measure near-IR reflectance spectra under martian atmospheric conditions. Six samples were studied that cover part of the diversity of Mars surface mineralogy: a hydrated ferric oxide (ferrihydrite), two igneous samples (volcanic tuff, and dunite sand), and three potential water rich soil materials (Mg-sulfate, smectite powder and a palagonitic soil, the JSC Mars-1 regolith stimulant). Sorption and desorption isotherms were measured at 243 K for water vapor pressure varying from 10^{-5} to ~0.3 mbar (relative humidity: 10^{-4} to 75%). These measurements reveal a large diversity of behavior among the sample suite in terms of absolute amount of water adsorbed, shape of the isotherm and hysteresis between the adsorption and desorption branches. Simultaneous in situ spectroscopic observations permit a detailed analysis of the spectral signature of adsorbed water and also point to clear differences between the samples. Ferric (oxy)hydroxides like ferrihydrite or other phases present in palagonitic soils are very strong water adsorbent and may play an important role in the current martian water cycle by allowing large exchange of water between dust-covered regions and atmosphere at diurnal and seasonal scales.

1. Introduction

The martian regolith is suspected to play a key role in the planet's global water cycle. In the regolith, water is present in the structure of hydrated minerals, adsorbed around or within mineral grains or as accumulations of ice in the subsurface. To get a precise idea of the impact of the regolith on the past and present water cycle, it is crucial to quantify the amount of water trapped into the different reservoirs as well as the dynamics of exchanges between regolith, atmosphere and cryosphere.

Orbital and in situ observations of the martian surface and subsurface have already revealed precious information about the presence and coverage of the different water reservoirs at present. The Mars Odyssey neutron and gamma-ray spectrometers demonstrated the presence of water ice within the first top layer of the regolith at latitude higher than around 50° in both Northern and Southern hemispheres (Boynton et al., 2002; Feldman et al., 2002; Mitrofanov et al., 2002). Concentration and burial depth of water ice in this martian permafrost show latitudinal variations and a manifest asymmetry between the two hemispheres (Feldman et al., 2004, 2008). The GRS instrument also highlighted tropical latitudes deposits containing up to 11% water by mass. Because water ice is not stable at these latitudes, this water is often considered as hydration water, either adsorbed on grain surface or present in the structure of nominally hydrous minerals (Feldman et al., 2004). The SHARAD/MRO sounding radar recently collected indirect evidence for substantial accumulations of water ice at tropical latitudes several meters beneath the surface (Holt et al., 2008; Plaut et al., 2008). Stability of these water ice reservoirs and amount of exchange with today's atmosphere is highly dependent on the properties of the regolith that lies between ice and atmosphere (Schorghofer and Aharonson, 2005). The OMEGA/Mex imaging spectrometer highlighted the presence of phyllosilicates and sulfates, respectively, formed during the Noachian and Hesperian eras (Bibring et al., 2006; Gendrin et al., 2005; Poulet et al., 2005). In addition, analysis of the 3-μm hydration absorption band revealed that this feature is present everywhere on the martian surface attesting to the overall presence of adsorbed and/or structural water at least in the upper few mm of the martian regolith. Jouglet et al. (2007) and Milliken et al. (2007) propose first order estimations of the minerals water content that range between 2% and 15%, increasing from equatorial to polar regions. Jouglet et al. (2007) also observed seasonal variations of surface water content by a few percent. Using the TES dataset, Kuzmin et al. (2007) document strong spatial and temporal variations of the

* Corresponding author. Fax: +33 4 76 51 41 46.
E-mail address: antoine.pommerol@obs.ujf-grenoble.fr (A. Pommerol).

0019-1035/$ - see front matter © 2009 Elsevier Inc. All rights reserved.
doi:10.1016/j.icarus.2009.06.013

amount of bound water in the regolith. The CRISM/MRO imaging spectrometer recently provided highly detailed observations of hydrated minerals discovered by OMEGA with improved spatial resolution (Bishop et al., 2008; Mustard et al., 2008; Wray et al., 2008). In situ analysis of the Gusev and Meridiani soils by Mars Exploration Rovers (MERs) confirmed the presence of highly hydrated minerals in these two locations, essentially in the form of hydrated sulfates (Squyres et al., 2004; Wang et al., 2006b; Campbell et al., 2008).

To understand the relationships between these different reservoirs in the regolith and the martian atmosphere and then get a better understanding of the role of the regolith in the water cycle, both experimental and modeling approaches are used. Parameters such as adsorption and desorption isotherms, specific surface area or adsorption and diffusion kinetics of the regolith have to be determined using experiments on analog materials and then included into physical models of water exchange.

Measurements of adsorption and/or desorption isotherms have been conducted under conditions representative of the martian conditions for a few Mars soils analogs. Adsorption properties of smectites were studied by Anderson et al. (1978), Zent and Quinn (1997), Zent et al. (2001), Bish et al. (2003), Frinak et al. (2005), Jänchen et al. (2006) and Chevrier et al. (2008). The same types of studies have been performed with basalt powder by Fanale and Cannon (1971), Zent and Quinn (1997) and Bryson et al. (2008), with zeolites by Bish et al. (2003) and Jänchen et al. (2006) and with palagonitic soils by Jänchen et al. (2009). Conditions of pressure, temperature and relative humidity as well as sample nature and texture are often different between these studies, making the comparisons between reported results quite difficult. Even by taking into account those differences, results are often in large disagreement. For the same environmental conditions, the amount of water adsorbed by similar samples can vary by one order of magnitude or more between data reported by different investigators (see discussion by Bryson et al. (2008) for basaltic powder and Frinak et al. (2005) for Na-rich smectite). Discrepancies between results can be attributed to different sample preparation processes (Frinak et al., 2005), uncontrolled sample texture (grain size distribution, density...) or even bias linked to measurement methods and protocols. Chevrier et al. (2008) and Bryson et al. (2008) perform measurements under a CO_2 atmosphere and discuss the possibility of discrepancy with previous measurements made under a pure H_2O atmosphere.

Adsorption properties of many more minerals are available in the literature for terrestrial conditions. These measurements are usually made at higher temperature than those relevant for the martian surface. Effect of temperature is extremely important for the calculation of the "water saturation pressure": P_s (Wagner and Pruss, 2002) but this first order effect is already accounted for when adsorption is treated as a function of "relative pressure": P/P_s, also referred to as "relative humidity (RH)" in the particular case of water. There are some inferred second order effects of temperature but those are usually minor. Frinak et al. (2005) demonstrate that the effects of temperature are negligible compared to those of relative humidity variations by comparing adsorption isotherms measured by different investigators in the temperature range: 222–298 K. Therefore, some adsorption behaviors described at terrestrial temperatures (usually 293–300 K) can be extrapolated to the martian temperature range whereas the possibility of extrapolation is not proven for other properties such as sorption and desorption kinetics. A lot of experimental results are published for smectites (e.g. Hensen et al., 2001; Likos and Lu, 2001; Dontsova et al., 2004; Rinnert, 2004; Salles, 2006; Salles et al., 2008). Adsorption and desorption isotherms and kinetics are studied versus a variety of parameters (cation nature, pore size distribution...) and very detailed hydration processes are described. Delmelle et al. (2005) report the water adsorption properties as well as the porosity pertinent parameters (specific areas and pore size distribution) of six volcanic ash samples. Weidler (1997) discusses the role of sample preparation protocol for measurement of adsorption properties on ferrihydrite. Values of specific areas and pore size distribution are reported.

Structural water can also play a primary role in water exchange between martian regolith and atmosphere (Kuzmin et al., 2007). The role of sulfates is especially important, as these hydrated minerals are abundant and widespread on Mars. Some of those structurally hydrated minerals (Mg- and Ca-sulfates) could be present under various hydration states depending on relative humidity. Phase diagrams and transition kinetics were recently investigated by Vaniman et al. (2004), Peterson and Wang (2006), Wang et al. (2006a) and Chou and Seal (2007) and discussed in terms of impacts on the seasonal and diurnal water cycle.

Diffusion rates of water vapor through regolith analogs have also been investigated in the laboratory. Chevrier et al. (2007) and Hudson et al. (2007) published values for the diffusion coefficients of water vapor through the JSC Mars-1 regolith simulant. Hudson et al. (2007) also report values for glass beads and fine silicate dust, Bryson et al. (2008) for basaltic powder and Chevrier et al. (2008) for smectite clay.

Those experimental results are particularly useful to constrain numerical models of water transport between atmosphere and regolith. Whilst water vapor diffusion at martian condition is fast ($D \sim 10^{-4}$–10^{-5} m^2/s^{-1}, Hudson et al., 2007), the presence of an adsorbing regolith can significantly slow down water transfer (Zent et al., 1993; Chevrier et al., 2008), and then influence the accumulation/sublimation rate of an underlying ice slab. For computational reasons adsorption needs to be neglected if one desires the determination of ground-ice stability as a response to long-term climatic variations (i.e. low versus high obliquity periods, Schorghofer, 2007). However, this is only valid if the adsorption equilibration time is smaller than the temporal variations of surface humidity. This hypothesis can be tested by kinetics measurements or/and calculations from the shape of the adsorption isotherms for martian regolith analog materials (Zent et al., 2001; Chevrier et al., 2008).

Infrared spectroscopy is a powerful tool to analyze mineral hydration, both in the laboratory on natural and synthetic samples or for purpose of remote sensing on planetary surfaces. Measurement of analogs near-infrared reflectance spectra under conditions representative of the martian surface has been the objective of different investigations. Bishop et al. (1994), Bishop and Pieters (1995), Prieto-Ballesteros et al. (2007) and Cloutis et al. (2007,2008) exposed various minerals to low temperature and/or low relative humidity, representative of the martian surface. Bishop and Pieters (1995) compare the near-infrared reflectance spectra of different Mars soil analogs under ambient lab conditions and under low pressure (0.3 mbar air, 1 mbar air or 1 mbar CO_2) and low temperature (around −40 °C). Studied samples are montmorillonites enriched in ferrihydrite and ferric sulfate as well as palagonitic soil. The authors note the sensitivity of the spectral features at 1.9, 2.2, 3 and 6 μm to the pressure and temperature conditions. Bishop et al. (1994) use the same methods to study the behavior of different types of smectites under reduced pressure environments. Results are used to propose absorption band assignments in the 1.4, 1.9 and 3-μm regions. They also discuss differences in the shape of the water spectral feature depending on the type of water (bound to cations, surface adsorption, interlayer...). Prieto-Ballesteros et al. (2007) report extensive measurements of magnesium sulfates spectra studied as functions of temperature (140–300 K), relative humidity and UV radiation. Published spectra only cover the 1–2.5 μm spectral range and behavior at longer wavelengths is not documented. Variations of reflectance

spectra permit to determine the stability fields of different types of Mg-sulfate that differ by their amount of structural water. A similar study was conducted by Wang et al. (2006a) using Raman spectroscopy instead of near-infrared. In a recent article, Cloutis et al. (2007,2008) report the behaviors of a large set of mineral reflectance spectra (spectral range: 0.4–5.2 μm) when samples are exposed to martian conditions (temperature: 20 °C, 660 Pa of CO_2 and UV radiations). Many minerals show evidence of dehydration during the exposure to martian conditions. Unfortunately, relative humidity in the simulation chamber was not measured. Rinnert (2004) uses a Diffuse Reflectance simulation chamber installed on an Infrared Fourier Transform Spectrometer (DRIFTS) to measure at the same time the adsorption isotherms and the near-infrared diffuse reflectance spectra over the spectral range of 1.25–2.5 μm. This setup is used to study the hydration process of swelling clays: thermodynamics provides the quantity of water sorbed into the mineral at a given relative pressure while the shape of spectral features provides information on the nature and location of sorbed water. In a similar way, Richard et al. (2006) study the kinetics of water desorption from mesoporous silica and magnesium oxide using the DRIFTS method and observe variations of the spectral features of sorbed water during the desorption sequence.

Thermodynamics properties of associations between water and minerals are crucial to determine the role of the regolith in the martian water cycle. Near-infrared reflectance spectroscopy has been demonstrated to be one of the most powerful methods to study the mineralogy and hydration state of planetary surfaces. For these reasons, we have built an experimental setup designed to perform at the same time these two types of measurements on martian analogs and under conditions representative of the martian surface. Results obtained with this unique setup are expected to complement results of previous experimental studies described above. In this article, we report the measurements of the near-infrared reflectance spectra of six martian analogs equilibrated with different values of water vapor pressure, from 10^{-5} to 0.3 mbar at a temperature of −30 °C. Chosen analogs are: martian regolith simulant JSC Mars-1, ferrihydrite, smectite, dunite, volcanic tuff and volcanic tuff/Mg-sulfate mixture. We present water adsorption and desorption isotherms as well as the corresponding reflectance spectra. Hydration kinetics are also measured and are compared using thermodynamics and spectroscopic descriptions.

2. Methods

2.1. Experimental setup

2.1.1. Reflectance spectrometer

All spectra are measured with the LPG spectro-gonio-radiometer (Brissaud et al., 2004). This instrument is a bidirectional visible and near-infrared reflectance spectrometer operating over the 0.4–4.8 μm spectral range. Instrument design is optimized to achieve a good photometric accuracy (<1%) under most of the measurement geometries. All spectra reported in this paper were measured using vertical incidence: $\theta_i = 0°$ and an emergence angle of $\theta_e = 30°$. The spectrometer is installed in a cold room at a temperature of −10 °C. Sample spectra are measured relative to commercial reference surfaces: Spectralon® (Labsphere Inc.) for the spectral range: 0.4–2.5 μm and Infragold® (Labsphere Inc.) for the spectral range: 2.5–4.8 μm. Corrections are applied to take into account minor absorptions in the Spectralon® spectrum and non-Lambertian behaviors of the Spectralon® and Infragold® surfaces (Bonnefoy, 2001). For all measurements presented in this paper, a spectral sampling of 0.02 μm was used. This value is consistent with the majority of hyperspectral datasets acquired on planetary surfaces. As we aim to use the spectra presented in this paper to interpret hyperspectral data of the Martian surface (OMEGA, CRISM), we have chosen this value of spectral sampling despite the fact that a higher spectral resolution could potentially help to better interpret the spectra. In those conditions, the measurement of a complete spectrum requires about 90 min. However, as we are mainly interested in hydration features, we often restricted the measured spectral range to 1.2–4.2 μm or 1.7–4.2 μm depending on the sample.

In addition to full spectra measurements, we also used the spectrometer to perform continuous measurements of the sample reflectance at one particular wavelength, in the hydration bands (either 3.10 or 1.92 μm). In this mode of measurement, one value was measured every second to get an insight into exchange kinetics.

2.1.2. Simulation chamber

A simulation chamber for adsorption measurements was designed and built as a complement to the reflectance spectrometer. Fig. 1 presents a scheme of the complete experimental setup: spectrometer, chamber and adsorption device. The empty volume inside the chamber is 181 mL.

2.1.2.1. Sample holder. Dimensions of the sample are constrained by reflectance spectroscopy requirements (size of the incident and emergent beams and need for an infinite optical depth). Sample diameter is 30 mm and sample thickness can vary between 1 mm and 10 mm. All measurements reported in this paper were obtained using a 1 mm thick sample holder to limit diffusion effects and minimize equilibration time. According to theoretical arguments and experimental checking, this sample thickness is sufficient to make negligible a potential contribution of the sample holder to the measured spectrum.

2.1.2.2. Optics. The simulation chamber is closed on its upper surface by a sapphire window that is 150 mm in diameter and 3 mm thick. Sapphire has excellent transmission and is spectrally featureless in the visible and near-infrared. However, light reflection on the window as well as multiple reflections between the sample and the window can affect the absolute values of reflectance measured. More problematic, multiple reflections also result in a small reduction of contrast between continuum and absorption bands in the sample reflectance spectra.

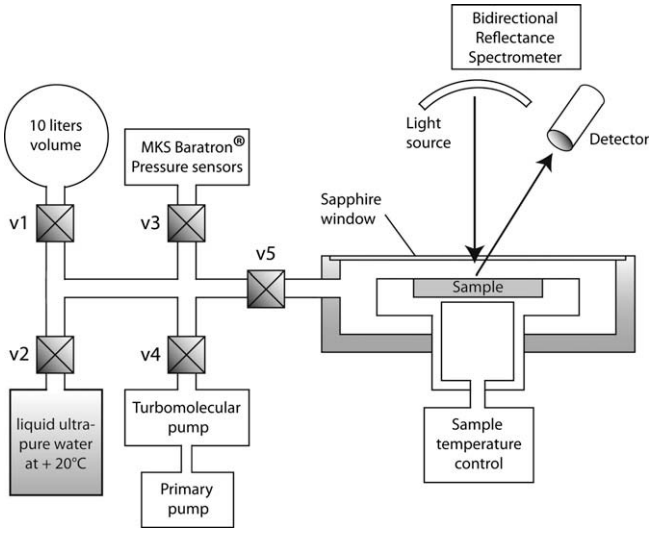

Fig. 1. Scheme of the experimental setup consisting of a bidirectional reflectance spectrometer, a simulation chamber containing the sample and an adsorption device. Each of the five valves is numbered to be easily identified in the experimental protocol description.

Therefore, we developed a simple model of multiple reflections between the sample and the sapphire window that we use to correct the measured spectra. In this model, we assume that when light encounters the sapphire window, a constant fraction of light, T, is transmitted in the forward direction while the complementary fraction of light, $1-T$, is reflected in the backward direction. We apply this assumption for all multiple reflections between sample and window, which gives the following relationship between the sample actual reflectance, R, and the apparent reflectance, M (measured with the window), at each wavelength:

$$M = T^2 \cdot R + (1-T) \cdot T^2 \cdot R^2 + (1-T)^2 \cdot T^2 \cdot R^3 + (1-T)^3 \cdot T^2 \cdot R^4 + \ldots = \sum_{i=0}^{\infty} (1-T)^i \cdot R^{i+1} \quad (1)$$

Application of this simple model to the data gives excellent results in correcting both the photometric bias and spectral effects of the sapphire window. Fig. 2 provides an example of the comparison between measurements made on the same sample without the window and with the window (raw and corrected). For this particular example, we choose an organic material that presents extremely contrasted values of reflectance in the visible and near-infrared spectral ranges to insure that the correction method is efficient from the lowest to the highest reflectance value.

2.1.2.3. Temperature control. Temperature of the sample is adjusted and controlled using a heating resistance, a Pelletier cooling system and a PT100 Platinum resistance thermometer placed directly under the bottom of the sample. A PID controller is used to program the sample temperature (fixed, ramp, cycles...). All measurements presented in this paper were made at a constant temperature of −30 °C. Prior to measurements, samples are dehydrated by maintaining temperature at +170 °C during several hours. In the same time, the sample holder and walls of the simulation chamber are maintained at high temperature (70–170 °C) under secondary vacuum to evacuate water and other trapped gases.

2.1.2.4. Vacuum. A turbo molecular pump is used to quickly pump the entire system to pressures lower than 10^{-6} mbar. During all experiments, an excellent static vacuum is required. Therefore, the whole system was optimized to avoid leaks and outgassing. When possible, only stainless steal Swagelok VCR® fittings qualified for ultra vacuum were used. The only exception is the simulation chamber that is assembled with three Viton® O-rings that did not present vacuum performance satisfactory for our purpose. Therefore we doubled every Viton® O-ring to permit an active pumping between the two concentric O-rings (classical "double O-ring" high vacuum fitting). Using this procedure and after consequent outgassing at high temperature and secondary vacuum, we obtain a high quality static vacuum (<10^{-6} mbar) than can be maintained in a close system at least for a few weeks.

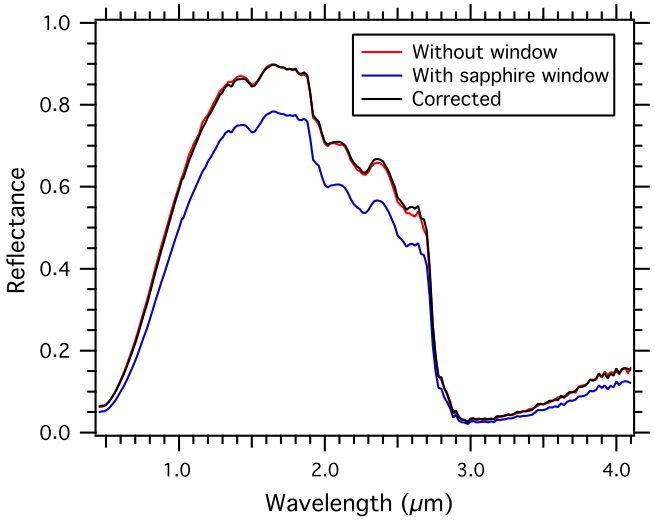

Fig. 2. Comparison between reflectance spectra of an organic material ("tholin") measured in the simulation chamber successively without (red curve) then with (blue curve) the sapphire window. Reflectance spectrum corrected from photometric and spectral effects of the sapphire window using Eq. (1) is also plotted in black. (For interpretation of the references to color in this figure legend, the reader is referred to the web version of this article.)

2.1.2.5. Pressure sensors. We use a MKS Baratron® absolute pressure sensor (range: 1 Torr) to monitor pressure inside the chamber. This particular sensor is able to measure pressure between 10^{-6} and 1 mbar. Relative uncertainty on the recorded value is highly dependant on pressure range: 50% at 10^{-5} mbar, 5% at 10^{-4} mbar, 0.5% at 10^{-3} mbar, 0.1% at 10^{-2} mbar and less than 0.1% at higher pressure. During injections or removals of water, pressure was measured every second while it was measured once every 20 s in the case of slow kinetics on long measurement periods (several hours and days).

2.1.2.6. Water vapor source. The source of water vapor is a volume of ultra pure, demineralised and carefully outgassed liquid water maintained at a temperature of +20 °C.

2.2. Samples description

Six different types of materials were studied. All of these materials are either suspected to be major mineral components of the martian regolith or are seen as good analogs of martian surface materials.

2.2.1. Regolith simulant JSC Mars-1

JSC Mars-1 is a "palagonitic" soil collected in a Hawaiian cinder cone (Allen et al., 1997). It is seen as a good spectral and magnetic analog to the martian surfaces materials (Allen et al., 1997, 1998). This material is largely amorphous or poorly crystalline. Main mineral components are Ca-Feldspar and magnetite. In the visible and near-infrared, its reflectance spectrum shows features attributed to ferric iron, OH^- and H_2O. One of the main discrepancies between the JSC Mars-1 analog and martian surface material is the very high water content of JSC Mars-1: mass loss of 21% at 600 °C (Allen et al., 1998). For this reason, spectral features attributed to H_2O are always more pronounced for the JSC Mars-1 analog than for the actual martian surface.

2.2.2. Ferrihydrite

Ferric oxides have been considered for decades as a major constituent of the martian dust and soil. A global map of "nanophase ferric oxide" has recently been published by Poulet et al. (2007) using OMEGA data. Comparison of this map with the global thermal inertia TES map (Putzig and Mellon, 2007) indicates that these materials are present everywhere fine dust accumulation is observed. In this class of minerals, we have chosen to analyze ferrihydrite, a quasi-amorphous (or nano-crystalline) iron (oxy)hydroxide. Associations between montmorillonite and ferrihydrite have been described as good spectral analogs of the martian surface in the near-infrared (Bishop et al., 1993) and observed as alteration products in the Lafayette meteorite (Treiman et al., 1993). Farrand et al. (2007) also consider ferrihydrite as well as other Fe^{3+} bearing minerals to interpret the visible and near-infrared spectra of Meridiani Planum soils measured by the Opportunity rover. We use a synthetic ferrihydrite powder described by Manceau and Gates (1997). Despite its abundance and widespread

presence on Earth, the structure of the mineral and the nature of water in ferrihydrite are still largely undetermined and debated. This is chiefly due to the extremely small size of individual particles (<10 nm) that make this mineral almost impossible to analyze with techniques such as XRD. Recently, Michel et al. (2007a,b) proposed a new model for the structure of ferrihydrite. Thermogravimetric analysis (TGA) reveals large amounts of physically adsorbed water (relative weight loss at 293 K of 17, 11 and 8% for respective particle size: 2, 3 and 6 nm). Considerable amount of water is also retained in the mineral at temperatures up to 700 K. This leads to the stoichiometry: $5Fe_2O_3{\cdot}nH_2O$ with $n = 10$, 6, 5 for respective average domain size: 2, 3 and 6 nm. However, the model proposed by Michel et al. (2007a) is in clear contradiction with other structural models such as the one proposed by Manceau and Gates (1997) where hydroxyl groups and not water molecule are present in the bulk of the structure.

2.2.3. Smectite SWy-2

Phyllosilicates and especially smectite clays have been suspected to be a major component of the martian dust and soils for decades (e.g. Hunt et al., 1973). This type of minerals was recently identified on Mars by the OMEGA mapping spectrometer (Poulet et al., 2005). Smectites are found in several locations of Noachian age on the planet's southern hemisphere. Due to very particular adsorption behavior associated with its swelling possibilities, smectite clays have been a popular subject of study by a number of investigators (see introduction for a few references). We use the sample SWy-2, a Na-montmorillonite purchased from the Clay Society Source Clay repository. Detailed analyses of this particular sample are reported in Costanzo and Guggenheim (2001) and companion articles. Our sample was dried sieved without grinding to separate different particle size fractions (see pictures in Pommerol and Schmitt, 2008a). Only the 25–50 μm particle diameter fraction is used in the present study. These "particles" are in fact agglomerates of the far smaller clay particles.

2.2.4. Dunite

Dunite is a magmatic rock containing more than 90 vol.% of olivine $(Mg, Fe)_2 SiO_4$. It also contains pyroxenes: $(Mg, Fe) SiO_3$ in smaller proportions. Olivine and pyroxenes are present on Mars as the main components (with feldspars) of volcanic deposits (tuff and lava flows). These minerals were identified and mapped by the ISM, TES and OMEGA instruments (Bibring et al. (1989), Bandfield (2002), Poulet et al. (2007)). We use a very fine dunite powder with particle size smaller than 25 μm.

2.2.5. Basaltic volcanic tuff

We have chosen a basaltic volcanic tuff as a good spectral analog of martian dust and soils in the visible and near-infrared. Especially, absorption features attributed to OH^- and H_2O in this sample give a better match with the ones observed by OMEGA on the martian surface than the JSC Mars-1 simulant, both in terms of strength and shape. The particular sample used in this study was collected in the volcanic province of Corent, Puy de Dôme, France. Visible and near-infrared spectra reveal absorptions features attributed to ferric iron, OH^- and H_2O. Macroscopic crystals of augite (a pyroxene of composition: $(Ca, Mg, Fe) SiO_3$) are disseminated in the red amorphous material. The sample was ground by hand and dry sieved to extract different particle size fractions (see pictures in Pommerol and Schmitt, 2008a,b). Only the 25–50 μm and 50–100 μm particle diameter fractions are used in the present study.

2.2.6. Magnesium sulfate

Large deposits of sulfate minerals have been observed from orbit by the OMEGA instrument (Gendrin et al., 2005) and in situ by the Opportunity rover in Meridiani Planum (Squyres et al., 2004). Since the identification of this family of hydrous minerals on the martian surface, the behavior of sulfate under Mars-like environmental conditions has been extensively studied in the laboratory (e.g. Vaniman et al. (2004), Wang et al. (2006a), Chou and Seal (2007), Chipera and Vaniman (2007)). We performed analyses using a sample of magnesium sulfate "heptahydrate" or epsomite: $MgSO_4{\cdot}7H_2O$ (Normapur grade, from Prolabo®). The sample was dry sieved without crushing to extract the 50–100 μm particle size fraction. Contrasting with other samples, we did not perform any measurement with pure Mg-sulfate. When pure sulfate is dehydrated at 170 °C, phase transition from heptahydrate to monohydrate results in a large variation of sample volume that modifies the texture of the sample surface in a way that is not suitable for reflectance spectroscopy purposes. Therefore, Mg-sulfate was mixed with basaltic volcanic tephra in mass proportions: 25%/75% to obtain a plausible analog of a sulfate-rich basaltic martian regolith (Squyres et al., 2004).

2.3. Experimental procedure

2.3.1. Sample preparation

Surface preparation protocol is crucial to obtain reproducible results, as reflectance in the visible and infrared spectral ranges is highly dependant on surface texture. The sample holder (diameter: 30 mm, thickness: 1 mm) is filled to rim with the non-compacted sample powder and then flattened with a spatula to obtain a smooth surface with limited powder compaction. In these conditions, mass of the samples ranges between 500 and 900 mg depending on the mineral intrinsic density and porosity.

2.3.2. Sample dehydration

The sample holder filled with the mineral powder is placed in the simulation chamber. The dehydration process is divided into successive steps that aim to remove the maximum amount of moisture from the sample while avoiding deterioration of its surface flatness (volume change and dehydration cracking). First, the sample is heated at 170 °C following a temperature ramp of 1 h while the chamber is still open to air. After 1 h of heating at 170 °C, the chamber is closed and heating stops. Sample temperature decreases for a few hours to reach the temperature of the cold room (−10 °C). Then, the simulation chamber is slowly pumped down to pressure lower than 10^{-6} mbar. Under secondary vacuum, the sample is heated again at 170 °C during a minimum of 10 h. In the same time, the chamber itself and fittings are heated using heating cords to ensure a quick and efficient outgassing. Finally, the sample is cooled to the temperature at which measurements are performed (−30 °C) and temperature is then kept constant (±0.1 °C) for the complete set of measurements.

2.3.3. Water sorption

In the initial state, the entire setup is under static high vacuum ($P < 10^{-6}$ mbar) after completion of the dehydration process previously described. Valves 1 and 3 remain open while valves 2, 4 and 5 are closed (see Fig. 1). Prior to any action, continuous reflectivity measurement at one wavelength inside a hydration band (either at 1.93 or 3.10 μm) as well as continuous measurements of pressure, sample temperature and room temperature are started.

A brief opening of valve 2 allows for liquid water evaporation and water vapor accumulation in the 10 L volume. After closure of valve 2, absolute pressure can be read using the Baratron® sensor. While valves 1 and 3 remain open, valve 5 is opened allowing adsorption of water vapor onto the sample. When equilibrium is reached (no significant temporal evolution of pressure and reflectance), continuous reflectance measurement at one wavelength is stopped and a reflectance spectrum is measured.

After completion of the full spectrum measurement, valve 5 is closed (valves 1 and 3 remain opened, valve 2 is closed) and the full procedure is repeated to obtain measurements for a new hydration step. The procedure is repeated until pressure at equilibrium after adsorption on the sample reaches a maximum value corresponding to a relative humidity of about 75%. This limitation in terms of relative humidity is imposed by the coldest point in the simulation chamber.

2.3.4. Water desorption

In the initial state, the sample is equilibrated with water vapor in the chamber and the rest of the setup. Valves 2 and 4 are closed while valves 1, 3 and 5 are open. Prior to any action, continuous reflectivity measurement at one wavelength inside a hydration band (either at 1.93 or 3.10 μm) as well as continuous measurements of pressure, sample temperature and room temperature are started.

Valve 4 is opened for a few minutes to lower pressure in the setup by pumping water vapor. Then, valve 4 is closed again and pressure increases due to sample dehydration until a new equilibrium is reached. At equilibrium, a full reflectance spectrum is measured. The full procedure is then repeated many times while progressively increasing the duration of active pumping.

2.3.5. Calculation of samples water content

Both thermodynamics and spectroscopy are used to determine the amount of water in the sample at each step of the hydration/dehydration process. For each adsorption step, the quantity of water adsorbed by the sample can simply be calculated by a mass balance considering the amount of water vapor introduced in the setup before adsorption, the amount of water vapor remaining in the simulation chamber from the previous hydration step and the amount of water vapor at equilibrium at the end of the current hydration step. We use the perfect gas law to convert absolute value of pressure in quantity of water. In the ranges of pressure and temperature of our measurements, considering water vapor as a perfect gas does not introduce severe bias in the mass balance (Burnett et al. 1996). However, the calculation requires a good knowledge of the different volumes, which were previously determined using helium expansion measurements from a standard volume. The temperature of the whole system also has to be very stable which was insured by the installation of the system in the cold room ($T = -10$ °C). Room temperature was continuously measured to avoid any potential bias associated with an unexpected variation of temperature. Potential adsorption of water elsewhere than on the sample would also induce a severe bias in the retrieval of the quantity of adsorbed water in the sample. As a test, we measured the adsorption isotherm of the empty chamber without any sample. The quantity of adsorbed water was found to be orders of magnitude lower than with an adsorbing sample in the chamber. Therefore, for moderately to strongly adsorbing samples, it seems reasonable to neglect these effects when calculating the quantitative adsorption isotherm. This situation may only become problematic with the least adsorbing samples at high relative humidity. In that case, only measurements at low to intermediate relative humidity are used to calibrate the spectroscopic method used for the rest of the adsorption branch and the entire desorption branch of the isotherm as detailed below.

Whereas it is possible to calculate water content directly from pressure measurements for the adsorption branch, such a measurement cannot be done for the desorption branch because the amount of water vapor pumped from the chamber is not measured. Therefore, we use spectroscopy to calculate the amount of water for the desorption branch. Milliken and Mustard (2005, 2007a,b) discuss the possibility to determine the amount of water in a mineral from the strength of its near-infrared absorption bands. The spectral criterion ESPAT defined by Hapke (1993) and calculated at 2.9 μm is found to be proportional to a mineral's water content. It is also independent of mineralogical and chemical composition (Milliken and Mustard, 2005) and is not affected by variations of reflectance in the spectral continuum (Milliken and Mustard, 2007a). However, the relationship between this parameter and water content is highly dependent on particle size (Milliken and Mustard, 2007b). We calculated the ESPAT parameter at 2.9 μm for each spectrum and compared these values to water content values calculated from pressure measurement in the adsorption branch. As expected from previously mentioned papers, we found a linear relationship between ESPAT and water content for all the samples. Furthermore, the slope of the linear correlation indicates values of particle size (using equation in Fig. 9 from (Milliken and Mustard, 2007b)) consistent with the values that were determined for all our samples. For example, the slope of the linear relationship between the amount of water adsorbed and the ESPAT parameter for smectite SWy-2 (Fig. 3) indicates a particle size of around 30–35 μm, consistent with the sieves openings (25–50 μm) used to extract the particles that compose the measured sample.

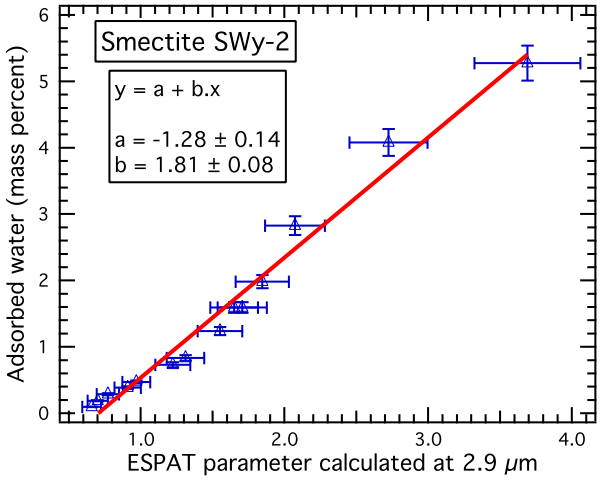

Fig. 3. Example of the relationship between the ESPAT parameter (as calculated by Milliken and Mustard, 2007a) calculated at 2.9 μm and the amount of water adsorbed in the sample. A clear linear relationship is observed and coefficients of the linear regression as well as corresponding uncertainties are indicated.

These results, using the ESPAT criterion, are used to obtain the quantity of water remaining in each sample after the initial dehydration process. To calculate the water content of the samples in the desorption branch, relationships between the Integrated Band Area (IBA) of the 3-μm absorption and the water content for each sample were derived. IBA calculated on the broad 3-μm band gives a better signal-to-noise ratio than ESPAT calculated at a single wavelength where absorption is close to saturation. However, contrary to ESPAT, the relationship between the IBA criterion and sample water content is highly dependent on sample mineralogy, chemistry and texture. Therefore, this quantitative relationship has to be established independently for each sample. Fig. 4 describes schematically how the spectral IBA criterion is calculated on reflectance spectra as well as spectra converted to single scattering albedo using Hapke equations (Hapke, 1993). First, a horizontal continuum is defined above the absorption band using measured value of reflectance or single scattering albedo at 2.20 μm. Then, discrete integration on the spectral range: 2.92–4.10 μm is used to determine both the area and the barycenter of the band. Let $R(\lambda)$ be the value of reflectance at the wavelength λ on the spectrum and $C(\lambda)$ the value of reflectance in the continuum. The Integrated Band Area (IBA) and barycenter (B) are calculated as follows:

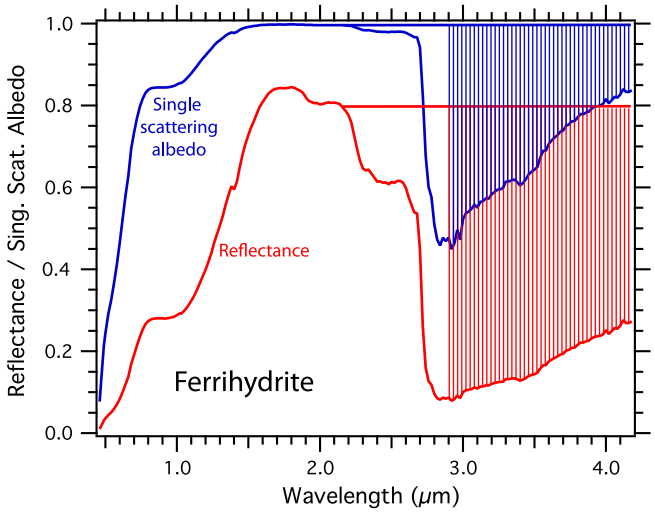

Fig. 4. Spectra of the dehydrated ferrihydrite measured in reflectance (red curve) and converted to single scattering albedo (blue curve). Continuums above the 3-μm absorption band and areas of the bands are schematically represented. Integration on reflectance spectra is used to determine absorption band intensity whereas integration on spectra converted to single scattering albedo is preferred for the calculation of band barycenter. (For interpretation of the references to color in this figure legend, the reader is referred to the web version of this article.)

$$\mathrm{IBA} = \sum_{i=\lambda_0}^{i=\lambda_1} C(i) - R(i) \tag{2}$$

$$B = \frac{\sum_{i=\lambda_0}^{i=\lambda_1}(C(i)-R(i))\times i}{\sum_{i=\lambda_0}^{i=\lambda_1}(C(i)-R(i))} = \frac{\sum_{i=\lambda_0}^{i=\lambda_1}(C(i)-R(i))\times i}{\mathrm{IBA}} \tag{3}$$

Note that for calculations of band barycenter, we applied the last formula on spectra converted from reflectance to single scattering albedo using equations from Hapke (1993). This conversion efficiently attenuates the effects of saturation in the 3-μm band (see Fig. 4). Polynomial functions were fitted to the data and then used to calculate samples water content for each step of the dehydration process. Fig. 5 presents empirical relationships obtained between the IBA spectra criterion and amount of water adsorbed for the six samples. Measurements are efficiently fitted by degree-3 polynomial functions. The coefficients of these functions with uncertainties on their determination ($1-\sigma$ error) are reported in Table 1.

2.3.6. Calculation of relative humidity

Relative pressure of water vapor, or relative humidity, is calculated from the water vapor absolute pressure P and the saturation pressure of water vapor P_s:

$$\mathrm{RH}\ (\%) = 100 * P/P_s \tag{4}$$

P_s is highly dependent on temperature T. We use the empirical relationship between P_s and temperature proposed by Wagner and Pruss (2002):

$$\ln\left(\frac{P}{P_n}\right) = 13.928169(1-\theta^{-1.5}) + 34.7078238(1-\theta^{-1.25}) \tag{5}$$

where: $\theta = T/T_n$ and $T_n = 273.16$ K and $P_n = 0.000611657$ Pa.

2.3.7. Estimations of measurements uncertainties

Because the measurements presented in this article make a quasi-systematic use of combined methods (spectroscopy and thermodynamics), the rigorous and accurate calculation of measurement uncertainties is particularly challenging. Furthermore, in most of measurements presented in this article, two kinds of errors must be distinguished: systematic errors that affect series of the measurements in a constant way (global shifting of an isotherm or a series of spectra) and relative errors affecting each point within a series of measurements (dispersion around a general trend).

To estimate both types of uncertainties in our measurements, we classified all possible sources of errors by order of importance. Uncertainties were obtained either from manufacturer specifications (Baratron pressure sensors, PID controller...) or by appropriate experimental procedures (same measurements repeated with and without samples, long term evolution of static vacuum...). Then, we propagated the uncertainties on each parameter in the calculation processes. We found two major sources of systematic errors. The first source of error is related to the adsorption of water vapor on surfaces other than the samples. As already mentioned, this error is maximal at high relative pressure and for the least adsorbing samples. From adsorption measurements conducted with no sample in the chamber, we concluded that the maximal uncertainty, in the worst case, is around 10% of the calculated water content value. The second major source of error is due to the possible thermal gradient in the sample holder. The temperature of the sample is then slightly larger than the one measured in the sample holder (by a few tenths of degrees). This small error on the measurement of the sample temperature has however a strong effect on the value of P_s used to calculate the relative pressure of water vapor. It leads to a relative uncertainty on the value of P/P_s estimated to be around 10% for a maximum error on the effective sample temperature of 1 °C. All other uncertainties are found to be far smaller, on the order of 1% of the measured values, and can therefore be neglected.

Uncertainties on spectral measurements are easier to quantify than uncertainties on water content or relative humidity. For each spectral measurement (i.e. for each wavelength), multiple data points are averaged and both a mean value and a standard deviation are calculated. Uncertainty on a measured value of reflectance is highly dependant on signal/noise ratio, correlated itself with the absolute value of reflectance. Thus, relative uncertainty for the very low values of reflectance measured at the maximum of absorption in the 3-μm band can reach around 5% whereas it is always far smaller than 1% in the continuum of the spectrum or inside weak absorption bands. However, when integrated spectral criteria like Integrated Band Area (Eq. (2)) or band barycenter (Eq. (3)) are calculated, the relative uncertainty drastically decreases and becomes negligible compared to uncertainties made on relative humidity and sample water content.

3. Results

3.1. Hydration Kinetics

Hydration kinetics is monitored for each water sorption or desorption step using both reflectance spectroscopy and pressure measurements. These two methods enable us to monitor the adsorption by both the bulk and the surface layers of the sample. On one hand, pressure in the chamber will vary as a function of the amount of water adsorbed in the totality of the sample. On the other hand, reflectance spectroscopy probes only the first few micrometers or tens of micrometers of the sample because we look at spectral features with high absorption coefficients.

Fig. 6 provides an illustration of the results obtained by the joint use of pressure and reflectance. For two different samples (basaltic tuff and ferrihydrite), the "average" sample water content is calculated from the simple mass balance between vapor and adsorbed water while "surface" water content is calculated from reflectance spectroscopy in the absorption band. Both methods provide water

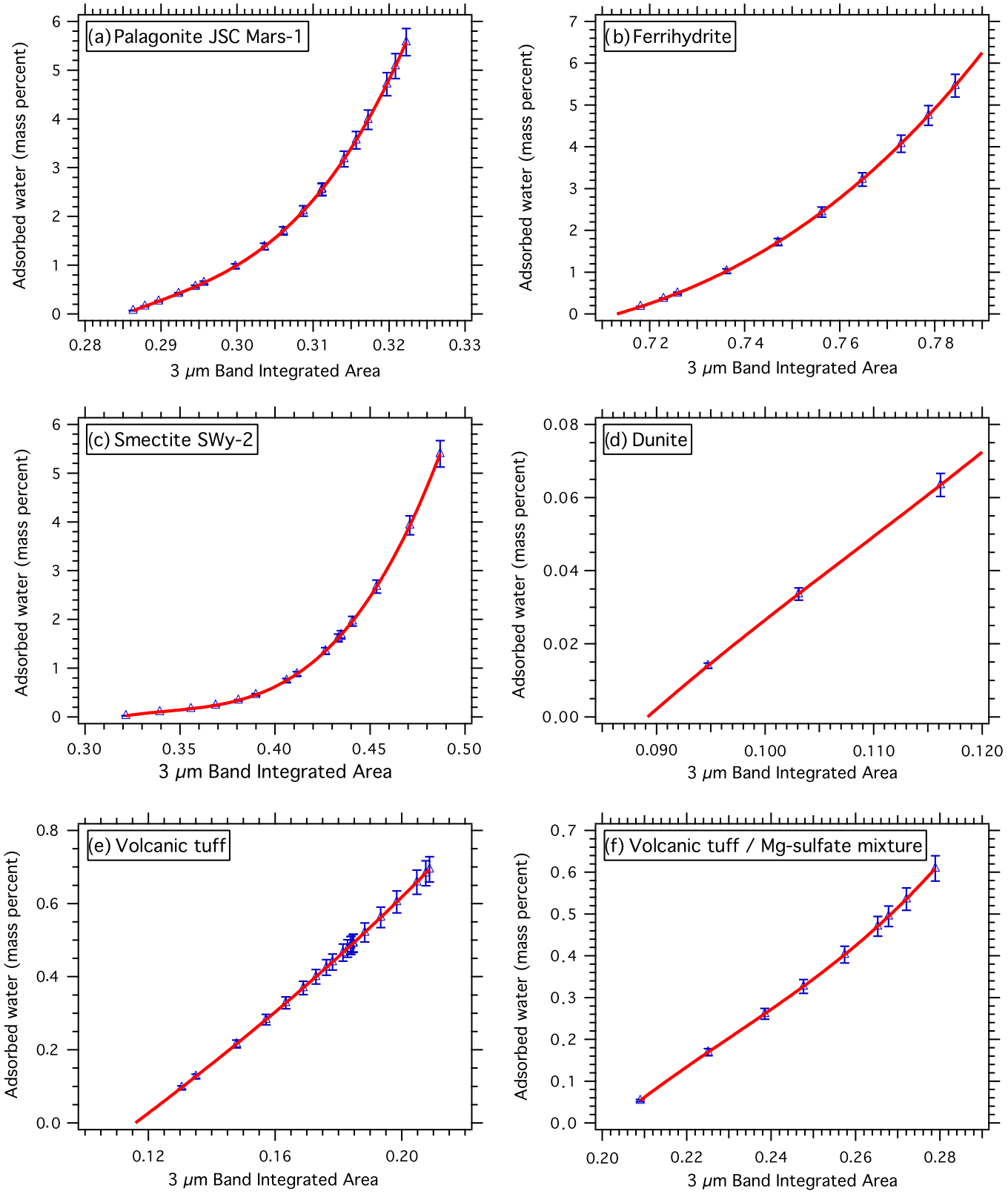

Fig. 5. Values of the Integrated Band Area of the 3-μm absorption band plotted as a function of the amount of water adsorbed for the six samples (a to f). Polynomial functions (degree 3) are fitted to measured points. Values of the obtained coefficients and corresponding uncertainties are presented in Table 1.

content values every second during the adsorption process. In the case of the volcanic tuff, "average" and "surface" water contents show simultaneous and similar variations. In a different way, the ferrihydrite sample shows a non-monotonic behavior of the surface water content that presents an almost instantaneous increase and then a slower decrease toward an equilibrium value. We interpret this behavior as an effect of the slow diffusion of the water from the top to the bottom of the sample as a response to the quick

Table 1
Coefficients of the polynomial empirical relationships established between the amount of water adsorbed on each sample and the value of the 3-μm Integrated Band Area (IBA). $y = K0 + K1\,x + K2\,x^2 + K3\,x^3$ where y is the amount of adsorbed water in weight percent and x the IBA spectral criterion. The $1-\sigma$ uncertainties are indicated for each parameter.

	Palagonite JSC Mars-1	Ferrihydrite	Smectite SWy-2	Dunite	Basaltic tuff	Mg-sulfate/basaltic tuff mixture
K0	−2073.1 ± 1.09	−640.25 ± 0.864	−65.685 ± 0.00269	−0.58762 ± 4.38e−5	−0.76567 ± 1.32e−4	−9.0554 ± 8.67e−4
K1	21480 ± 10.7	2950.6 ± 3.45	568.1 ± 0.0202	12.996 ± 0.00111	7.316 ± 0.00247	107.03 ± 0.0108
K2	−74378 ± 35.3	−4544.1 ± 4.59	−1645.3 ± 0.0503	−98.98 ± 0.00917	−11.854 ± 0.0152	−435.28 ± 0.0442
K3	86077 ± 38.6	2335.5 ± 2.04	1598.6 ± 0.0413	304.34 ± 0.0248	49.279 ± 0.0306	630.28 ± 0.0604

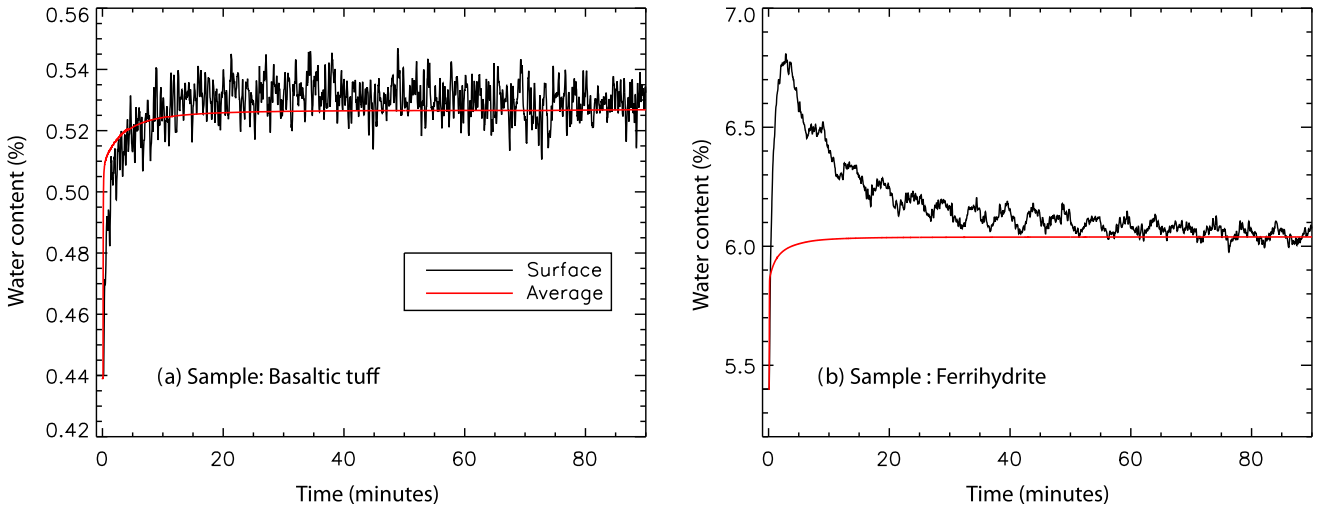

Fig. 6. Sorption kinetics measured by reflectance spectroscopy and thermodynamics (volumetric calculation). Spectroscopy probes the first upper grains of the sample ("surface", black curve) while thermodynamics indicates the global, integrated vertically, water content of the sample ("average", red curve). Examples of the volcanic tuff (a) and ferrihydrite samples (b), two samples that show very different behaviors. Relative humidity at equilibrium is 10^{-2} in each case. (For interpretation of the references to color in this figure legend, the reader is referred to the web version of this article.)

increase of water vapor pressure in the chamber and instantaneous adsorption on the first top grains. Such vertical gradients of adsorbed water are only visible for the two samples that adsorb large quantities of water: ferrihydrite and JSC Mars-1. Other samples do not show evidence of such vertical gradients of water content.

The combined use of these two methods also provides precious pieces of information on the dependence of adsorption, desorption and diffusion with relative pressure. Detailed results and discussions regarding the kinetics of water exchange with the six analog samples will be provided in a separate paper.

3.2. Adsorption and desorption isotherms

Figs. 7 and 8 show the adsorption and desorption isotherms for the six samples. In a classical way, water content is plotted versus P/P_s (or "Relative Humidity), both in linear and logarithmic units. While the linear P/P_s scale is useful to compare measured isotherms to those of published reference materials (e.g. Gregg and Sing, 1982), a logarithmic P/P_s scale is more appropriate for discussion regarding the case of the martian surface for which extreme variations of P/P_s are encountered. At 243 K (−30 °C), saturation pressure of water is: $P_s = 0.37$ mbar (empirical relation from Wagner and Pruss, 2002).

For all the samples, the dehydration process consisting of outgassing under secondary vacuum at 443 K for 10 h was unable to remove the totality of the water. Under those conditions, all the adsorbed water was removed and only chemically bound or structural water or hydroxyl remains stable. The amount of this type of water is extremely variable among the six samples. Table 2 summarizes the sample water/hydroxyl content after dehydration.

Maximum water content reached at the end of the successive adsorption steps is also reported in Table 2. We observe a very large variability in the amount of water adsorbed by the different materials, from less than 0.2% (dunite) to more than 6% (ferrihydrite). Despite the large differences in the amount of water adsorbed by the different samples, the shapes of the isotherms appear relatively similar for all the materials except smectite SWy-2. In the latter case, we observe a limited convexity toward the pressure axis while all other samples show a larger convexity in the opposite direction (in linear-axis plots). For all other samples than smectite, differences in the shapes of the isotherms are found in the ratio of relative variations between low (<0.1) and high (>0.1) relative pressure and in the shape of the "knee" between these two domains. The shapes of the isotherms are described in more details and compared to the classical isotherms of the BDDT classification (Brunauer et al., 1940) in the discussion section. These types of isotherm shapes and variability are correctly handled by the BET model (Brunauer et al., 1938) for relative pressure between 0.05 and 0.35 (Gregg and Sing, 1982). Therefore, we performed BET fits on all the isotherms including the smectite SWy-2. In all cases, quality of the fit is very satisfactory but the smectite SWy-2 shows more dispersion than other samples. Fig. 9 presents these BET fits for the six samples while Table 3 summarizes the fit parameters and results in terms of water adsorption properties.

BET parameters highlight differences between samples both in terms of specific adsorption area and energy distribution of the absorption sites. These values are compared to other values from the literature in the discussion section.

Noticeable hysteresis between adsorption and desorption isotherms are observed for all the samples. At the same value of water vapor pressure, strength of the band is always larger on the desorption branch than on the adsorption branch. This hysteresis is more or less developed depending on the sample. Furthermore, for most of the studied minerals, this hysteresis persists at very low relative

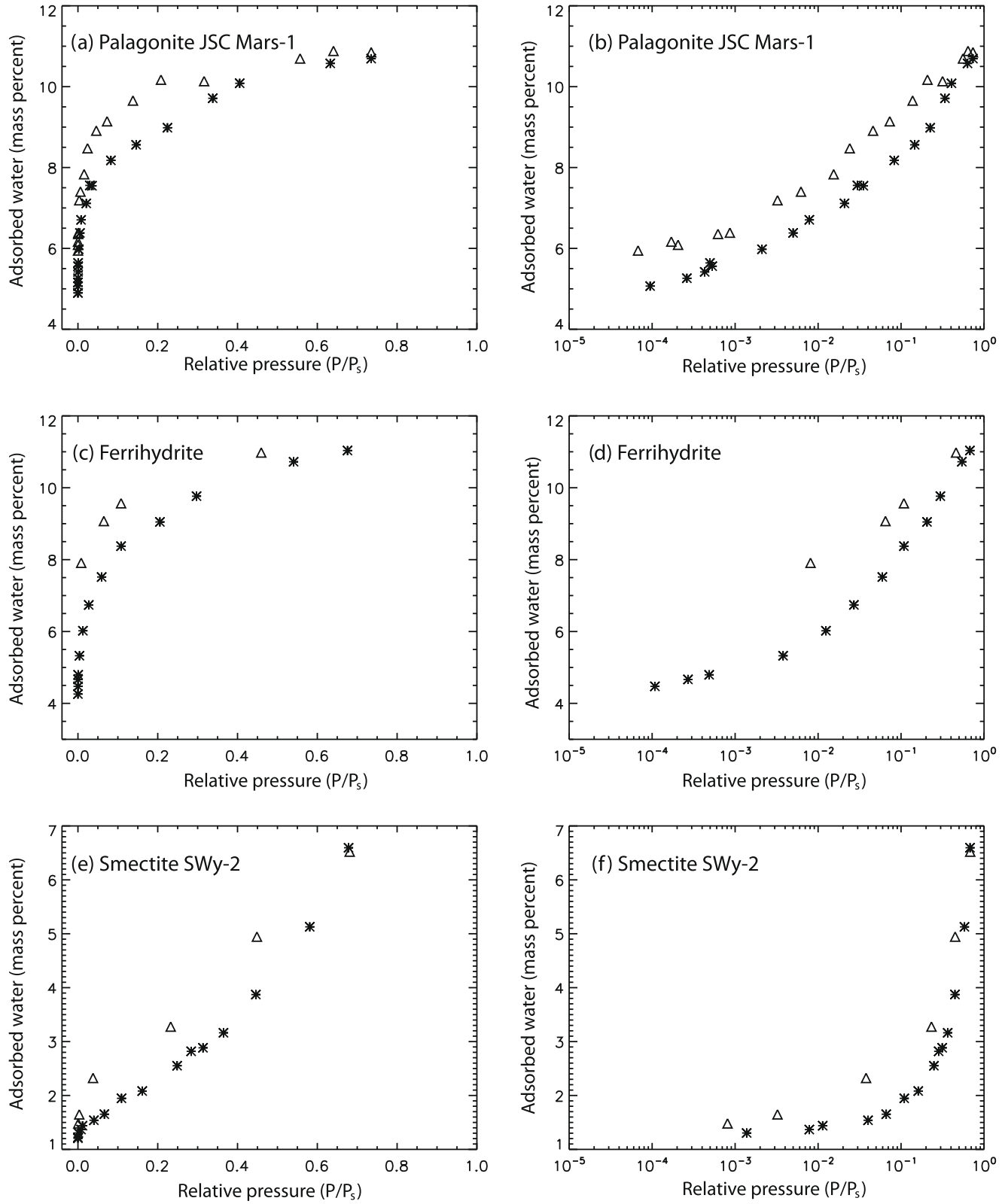

Fig. 7. Adsorption and desorption isotherms (stars and triangles, respectively) at −30 °C for three samples (a to f): JSC Mars-1, ferrihydrite and smectite SWy-2. For each sample, the relative mass of adsorbed water is plotted versus relative water vapor pressure in linear and logarithmic scales (respectively, left and right columns). Relative uncertainty on both water content and relative pressure is estimated to be 10%.

pressure. We tested the hypothesis that the observed so-called "hysteresis" was in fact only an effect of a very slow desorption kinetics. The time interval between the measurements of two successive spectra (consecutive to two successive water removal steps) was increased up to more than 3 days in the case of the JSC Mars-1. No visible variations of band strength resulted from this increased equilibration time. Finally, we tested the stability of the remaining water after the complete adsorption–desorption

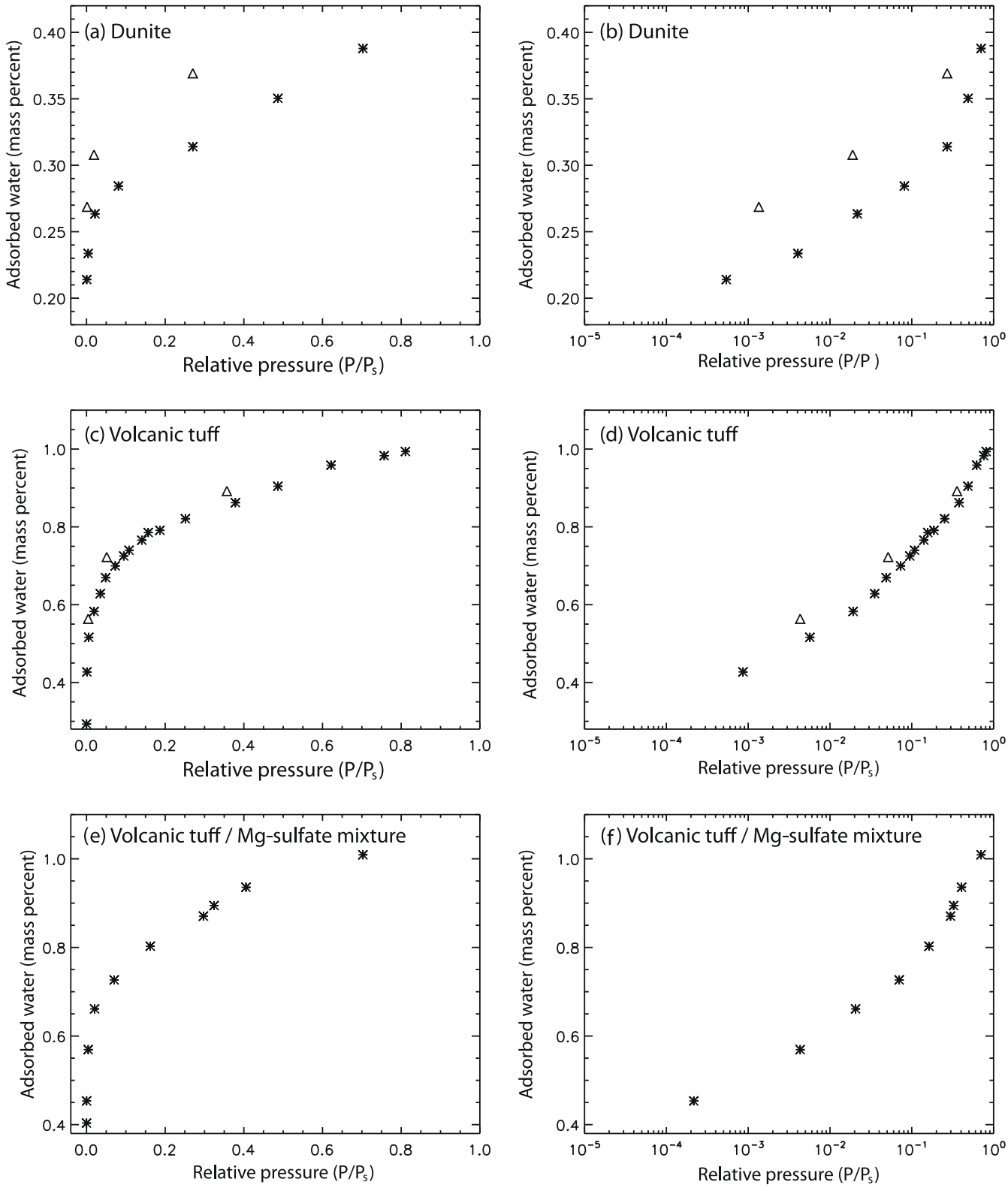

Fig. 8. Adsorption and desorption isotherms (stars and triangles, respectively) at −30 °C for three samples: dunite, volcanic tuff and Mg-sulfate/volcanic tuff mixture. For each sample, the relative mass of adsorbed water is plotted versus relative water vapor pressure in linear and logarithmic scales (respectively, left and right columns). Relative uncertainty on both water content and relative pressure is estimated to be 10%.

cycle. Sample temperature was increased up to +20 °C by steps of 10 °C. No change in the strength or shape of the hydration bands was visible. For other samples, equilibration time for the last points of the desorption hysteresis were also increased to at least 12 h and up to a few days but samples were always maintained at −30 °C and the effect of temperature increase was not tested. Thus, we conclude that these hysteresis effects are not entirely due to effects of slow desorption kinetics but may be largely due to a

Table 2
Water content (in weight percents) of the six samples after the dehydration process and at the end of the successive adsorption steps. Note that the determination of the initial water content, entirely based on spectroscopy, does not allow for the distinction between molecular water (H_2O) and hydroxyl (OH^-). Therefore, in that case, water content should be understood as water + hydroxyl content.

	JSC Mars-1 (%)	Ferrihydrite (%)	Smectite SWy-2 (%)	Dunite (%)	Volcanic tuff (%)	Tuff + Mg-sulf. (%)
After dehydration	5.0	4.3	1.2	0.2	0.3	0.4
After hydration	10.7	11	6.6	0.4	1.0	1.0

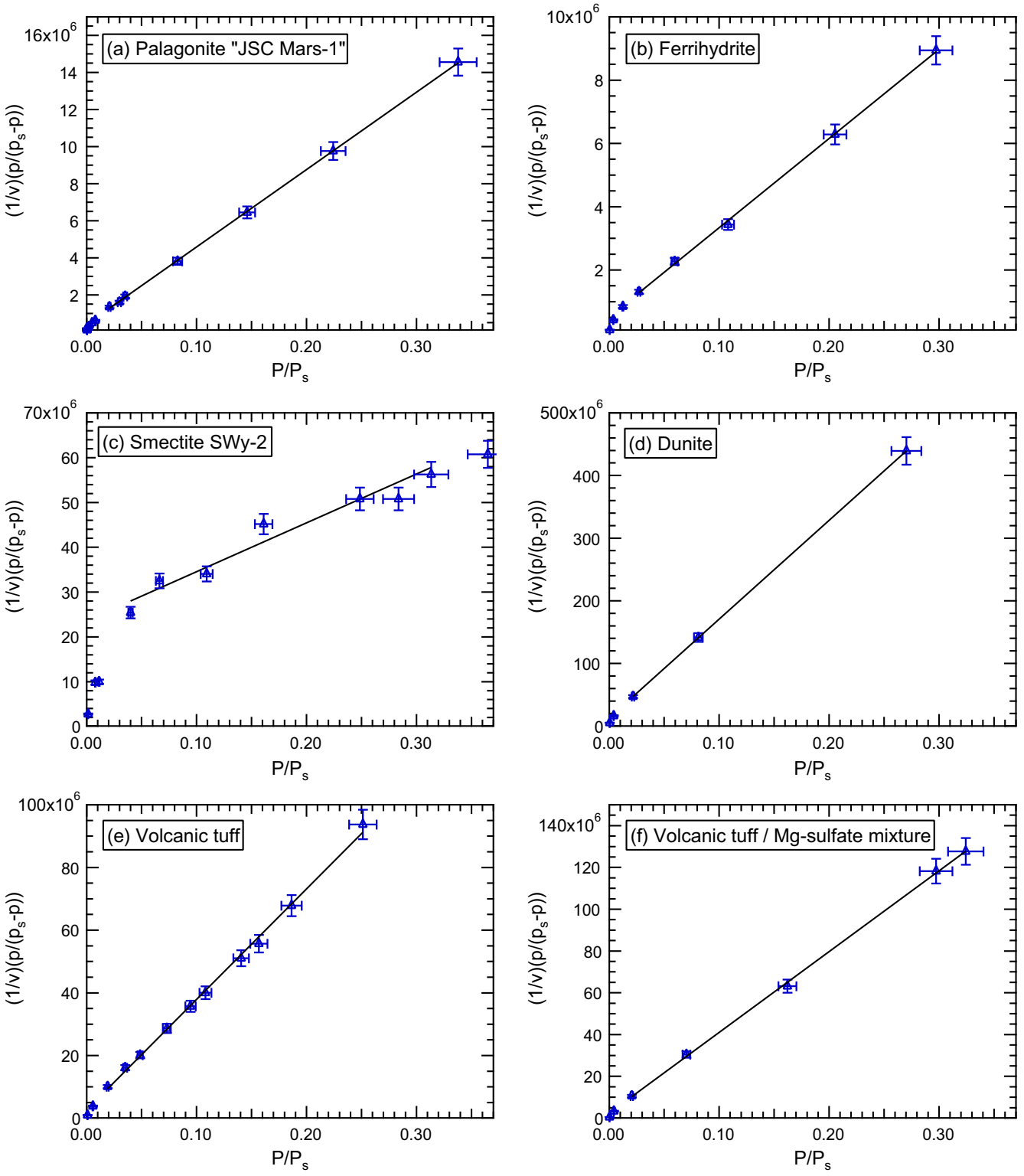

Fig. 9. BET fits for all the samples. Data are usually fitted for relative humidity between 0.05 and 0.35 as recommended by Gregg and Sing (1982). However, the domain of linearity often extends to lower relative pressure, down to 0.01 with most samples.

Table 3
BET parameters estimated by fitting the adsorption isotherms of the six materials for partial pressure ranging between 0.05 and 0.35. $K0$ and $K1$ are the coefficients of the linear regression in BET space: $y = K0 + K1 \cdot x$ where $y = (1/v)(p/(p_s - p))$ and $x = p/p_s$ (Fig. 9). V_m is the volume of the water monolayer normalized by sample mass: $V_m = (1/(K0 + K1))/m_{sample}$ (Brunauer et al., 1938). C is the BET adsorption constant and is calculated as: $C = 1 + K1/K0$ (Brunauer et al., 1938). SSA is the Specific Surface Area (normalized by sample mass), calculated by dividing the volume of the water monolayer: V_m by the thickness of a water monolayer: $t = 3 \times 10^{-10}$ m (Chevrier et al., 2008). The $1-\sigma$ absolute uncertainties are indicated for each calculated values.

	JSC Mars-1	Ferrihydrite	Smectite SWy-2	Dunite	Volcanic tuff	Tuff + Mg-sulf.
$K1$	$4.17 \times 10^7 \pm 1.9 \times 10^5$	$2.82 \times 10^7 \pm 4.2 \times 10^5$	$1.09 \times 10^8 \pm 1.1 \times 10^7$	$1.58 \times 10^9 \pm 1.9 \times 10^6$	$3.52 \times 10^8 \pm 6.2 \times 10^6$	$3.87 \times 10^8 \pm 4.9 \times 10^6$
$K0$	$4.10 \times 10^5 \pm 3.2 \times 10^4$	$5.20 \times 10^5 \pm 7.2 \times 10^4$	$2.36 \times 10^7 \pm 2.1 \times 10^6$	$1.32 \times 10^7 \pm 3.1 \times 10^5$	$2.64 \times 10^6 \pm 8.2 \times 10^5$	$2.41 \times 10^6 \pm 1.0 \times 10^6$
V_m (m^3/kg)	$3.19 \times 10^{-5} \pm 1.7 \times 10^{-7}$	$4.02 \times 10^{-5} \pm 6.9 \times 10^{-7}$	$1.58 \times 10^{-5} \pm 1.6 \times 10^{-6}$	$8.48 \times 10^{-7} \pm 1.2 \times 10^{-9}$	$4.10 \times 10^{-6} \pm 8.1 \times 10^{-8}$	$3.38 \times 10^{-6} \pm 5.1 \times 10^{-8}$
C	103.4 ± 8.4	56.5 ± 8.5	5.7 ± 0.9	120.8 ± 3.0	149.4 ± 48.4	196.0 ± 82.9
SSA (m^2/kg)	$1.06 \times 10^5 \pm 5.6 \times 10^2$	$1.34 \times 10^5 \pm 2.2 \times 10^3$	$5.27 \times 10^4 \pm 5.2 \times 10^3$	$2.83 \times 10^3 \pm 3.9$	$1.37 \times 10^4 \pm 2.7 \times 10^2$	$1.13 \times 10^4 \pm 1.7 \times 10^2$

bounding of water molecules or hydroxyl groups in some particular sites of the samples.

3.3. Near-infrared reflectance spectra

Figs. 10–15 present the reflectance spectra of each of the six materials equilibrated with different values of water vapor pressure. Values of relative pressure (P/P_s) at equilibrium are provided for each spectrum. Note that for clarity reasons, all the measured reflectance spectra are not represented. When a few spectra were measured at very similar values of relative pressure, only one of these spectra is presented. Therefore, there are more points plotted in the adsorption isotherms (Fig. 7 and 8) than spectra presented in Figs. 10–15.

As a response to large adsorption of water onto the samples, spectral features associated with water of hydration present a large variability for all samples. During successive adsorptions of water, an increase of the 3-μm band strength is evident for all the minerals. On the long-wavelength wing, it is clear for all studied minerals that the absorption by sorbed water extends far beyond 4 μm, up to 4.2 μm as this is visible on presented spectra but even up to 4.7 μm (additional spectral data, not shown here). On the short wavelength wing, weak absorption is visible between 2.35 and 2.55 for all samples except dunite. Spectral behavior of the samples between 2.55 and about 2.7 μm is hard to describe because of the absorption by water vapor around 2.6 μm. The maximum of absorption by water in the 3-μm band appears to be located around 2.9 μm. Between 2.7 and 2.9 μm, the shape of the H_2O band is sometimes altered by the absorption band of hydroxyl ions (OH^-) located at 2.75 μm that is dominant in this spectral region for the smectite and volcanic tuff samples. Both spectral features attributed to OH^-, at 2.2 and 2.75 μm, remain remarkably stable during water sorption in the case of the Swy-2 smectite. In the case of the volcanic tuff, as more and more water is adsorbed on the sample, absorption by H_2O progressively masks absorption by OH^- at 2.75 μm. In a very similar way, absorption band attributed to organic contaminants at 3.4 μm is almost entirely masked by the long-wavelength wing of the 3-μm H_2O band. For the SWy-2 smectite, we observe the same behavior with the weak band of carbonates (minor contaminant) at 4 μm. At 1.4 μm, absorption by H_2O overlaps an absorption by OH^-. As the absorption by H_2O occurs at longer wavelengths compared to OH^-, the long-wavelength wing of the OH^- band is affected by water adsorption while its short wavelength wing is not affected at all.

An important increase of the 1.9-μm band strength is also clear for the JSC Mars-1, ferrihydrite and smectite samples while it is barely visible for the volcanic tuff, pure and mixed with Mg-sulfate. However, no absorption at 1.9 μm is visible on the dunite spectra, even close to water saturation pressure. Shifts in the position of

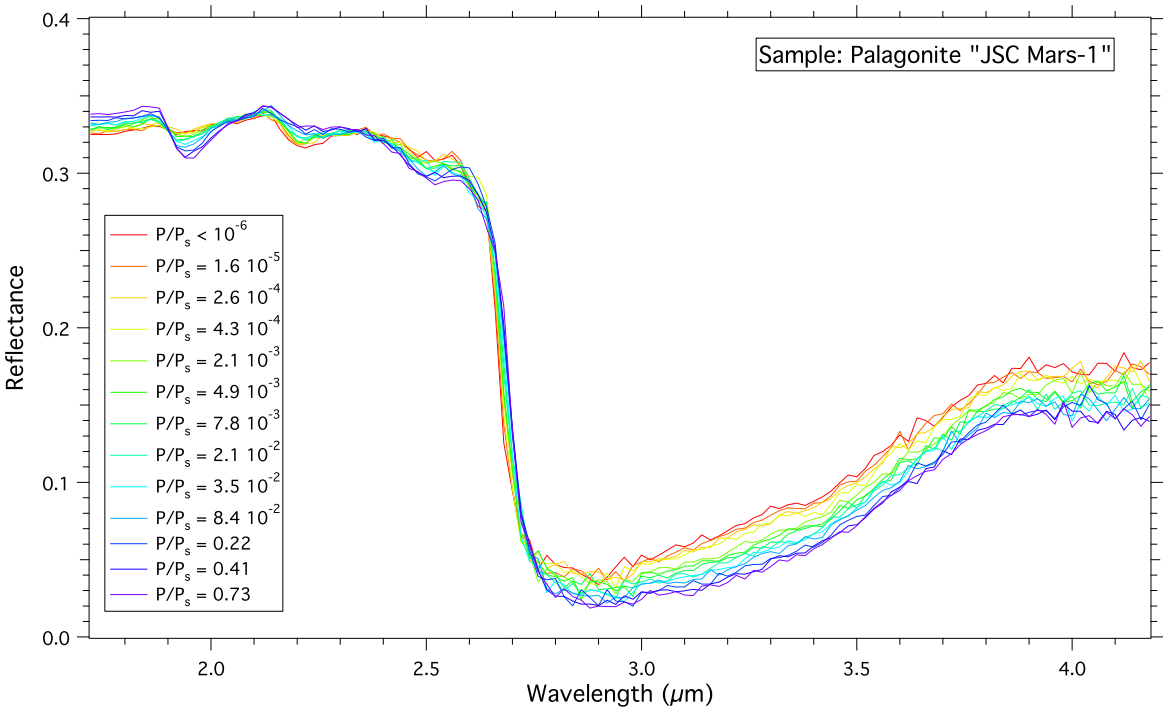

Fig. 10. Reflectance spectra of the palagonite "JSC Mars-1" measured under different values of water vapor relative pressure.

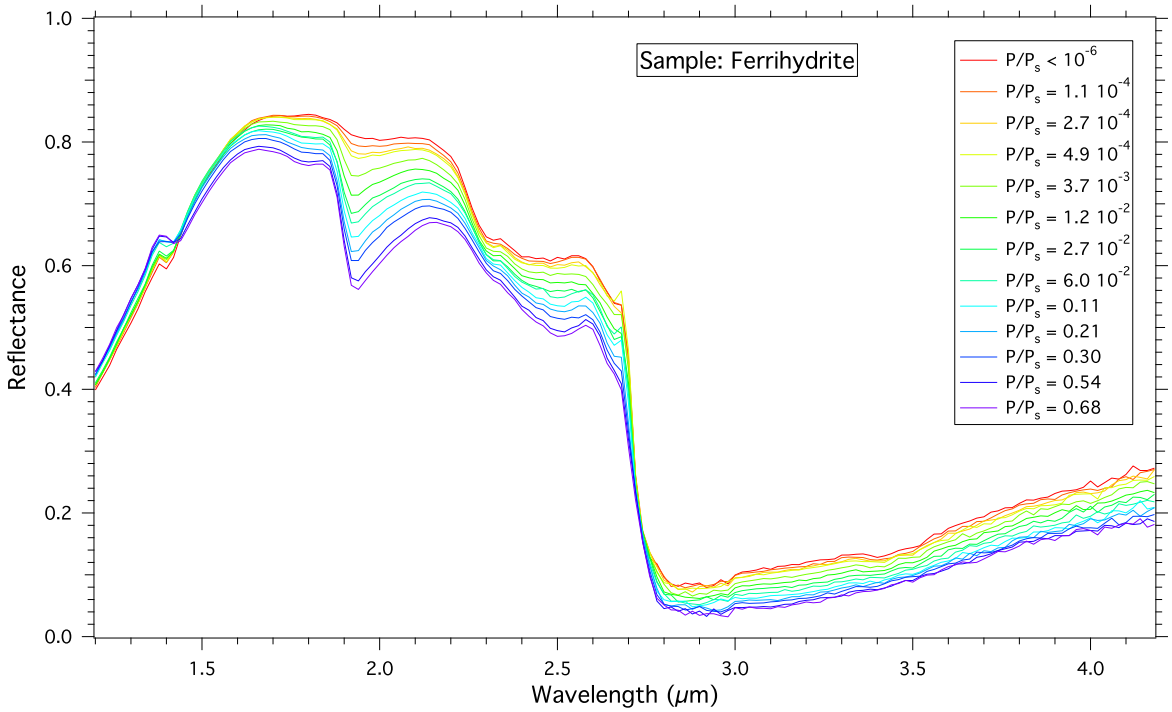

Fig. 11. Reflectance spectra of the ferrihydrite sample measured under different values of water vapor relative pressure.

the maximum of absorption and changes in the shape of the band are directly visible on some series of spectra. Those spectral effects are highlighted in the discussion section by calculation of spectral ratios between spectra of the same material with different hydration states.

Apart from the evolution of absorption bands attributed to water of hydration, modifications in the continuum of the spectra can be observed for JSC Mars-1 and ferrihydrite. We attribute these modifications in the continuum to physical variations of the sample during hydration (volume, porosity...). During the initial high temperature dehydration, changes were observed only for these two samples, essentially in the form of a volume decrease. Therefore, it seems very consistent that spectral changes in the continuum are observed for the same two samples: overall albedo changes are due to variations of samples textures during hydration and dehydration. However, a fundamental distinction has to be

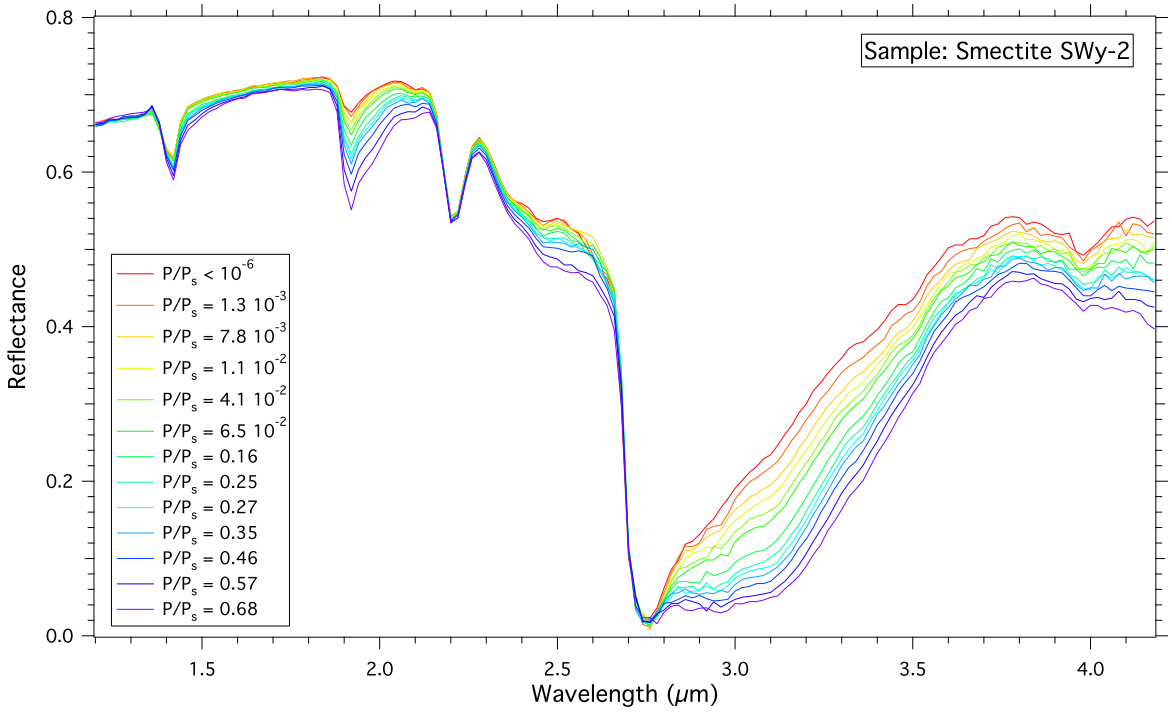

Fig. 12. Reflectance spectra of the smectite SWy-2 sample measured under different values of water vapor relative pressure. Data between 2.55 and 2.8 μm are not plotted because they are disturbed by variations of atmospheric water vapor in the room.

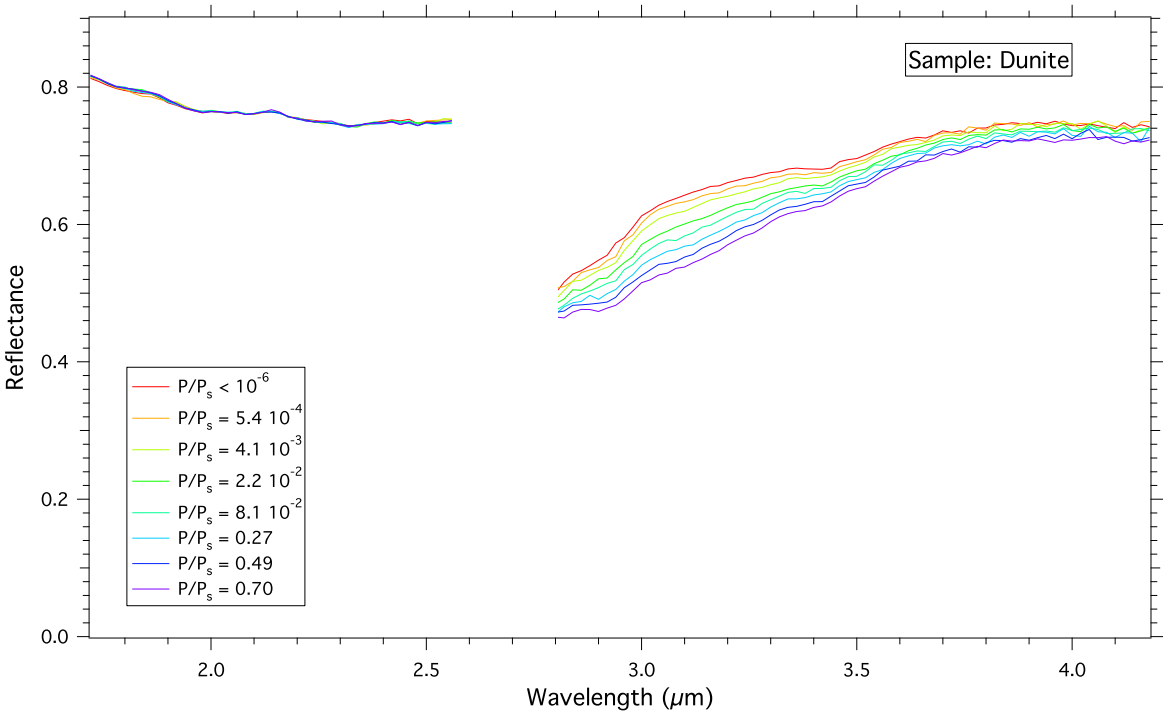

Fig. 13. Reflectance spectra of the dunite sample measured under different values of water vapor relative pressure.

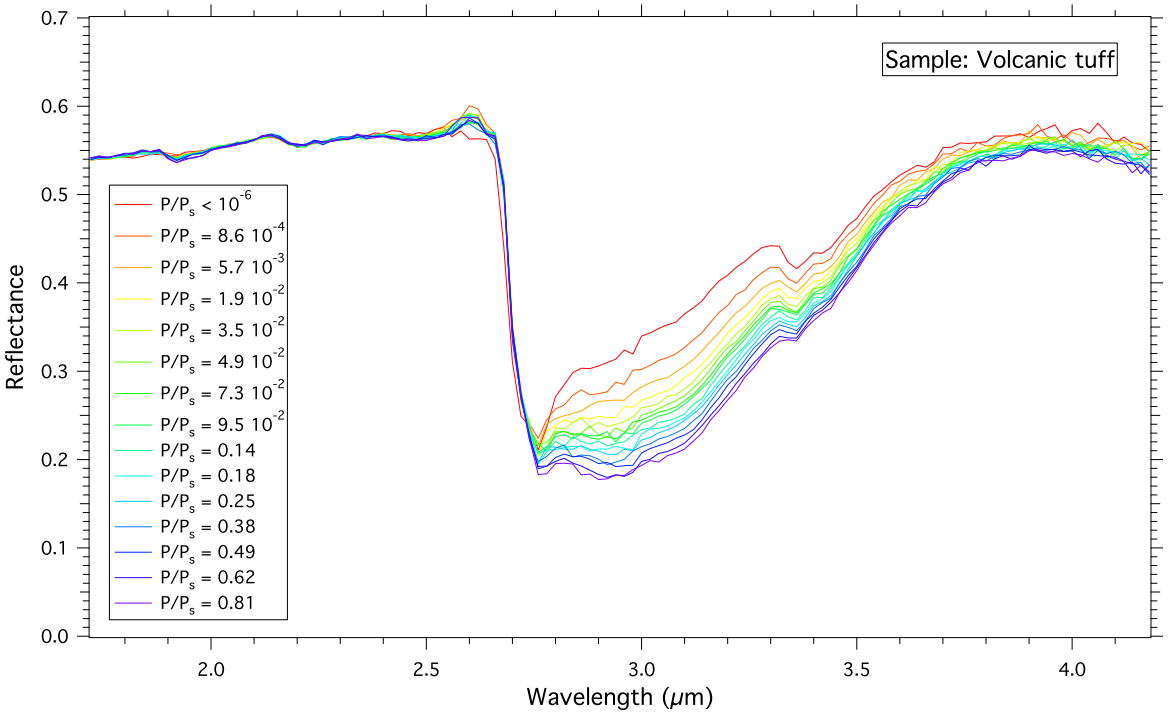

Fig. 14. Reflectance spectra of the volcanic tuff sample measured under different values of water vapor relative pressure.

made between the behaviors of ferrihydrite and JSC Mars-1. For the JSC Mars-1 sample, the level of reflectance in the continuum is maximal for the sample with the highest water content. This is visible at 1.8 and 2.1 μm on the spectra plotted in Fig. 10 but is also true at shorter wavelengths in the near-infrared and in the visible spectral ranges (complementary spectral data for the 0.5–1.8 μm range, not shown here). Ferrihydrite also presents a maximal level of reflectance in the continuum for the highest amount of sorbed water in the spectral range 0.5–1.4 μm. However, at longer wavelengths (1.4–4.7 μm), reflectance always decreases as water content increases even between the classically defined H_2O absorption bands. Furthermore, a strong slope develops toward long wavelengths as water adsorbs on the sample. We attribute this spectral effect to the broad absorption by water as described by Bishop et al. (1994) that competes with the opposite effect of texture change resulting in a global albedo variation.

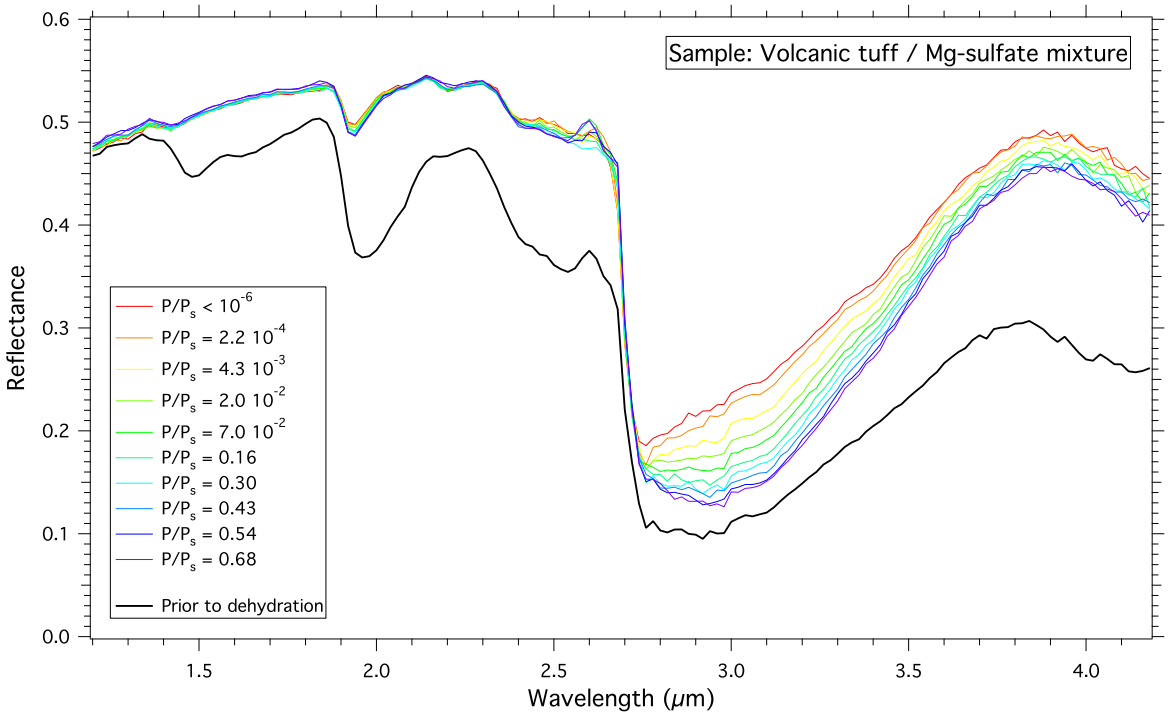

Fig. 15. Reflectance spectra of the Mg-sulfate/volcanic tuff mixture sample measured under different values of water vapor relative pressure.

In the case of the Mg-sulfate/volcanic tuff mixture, we also plot the spectrum of the sample prior to any dehydration. Mg-sulfate introduced in the mixture is epsomite ($MgSO_4{\cdot}7H_2O$). After dehydration at 170 °C under secondary vacuum, a less hydrated phase is obtained. Comparison with published reflectance spectra (Bonello et al., 2005) suggests the kieserite phase ($MgSO_4{\cdot}H_2O$). During the successive hydration steps, evolution of reflectance spectra shows sorption of water onto the sample but does not indicate any phase change of the Mg-sulfate (stability of the 1.9 μm and other weak bands). Total elapsed time from the first to the last water injection was 4 days. After this time, water vapor pressure was buffered at $P = 0.27$ mbar (relative humidity: RH = 73%) during 6 days. The spectrum measured after this long exposure to a wet atmosphere did not reveal any phase change of the Mg-sulfate. This observation suggests very slow kinetics for the monohydrated to polyhydrated phases transitions at 243 K, unlikely to influence the diurnal water exchange between regolith and atmosphere.

4. Discussion

The two types of measurements used in this study, spectroscopy and thermodynamics, reveal a manifest diversity in the interactions between the six proposed martian analogs and water vapor. This diversity is found from the comparisons between the different samples but also for a given sample when studying different domains of relative pressure.

4.1. Adsorption isotherms

Adsorption and desorption isotherms for the JSC Mars-1, ferrihydrite, dunite, volcanic tuff, pure and mixed with Mg-sulfate, present similar general shapes. In the "BDDT classification" of adsorption isotherms (Brunauer et al., 1940), isotherms of these five materials can be classified as type II, corresponding to non porous particles with eventually a contribution of type I, corresponding to the presence of micropores (width < 2 nm according to IUPAC definition). Type II corresponds to physical adsorption of water molecules on the surface of nonporous solids. The shape of this type of isotherm is described by the BET model for relative pressure in the range: 0.05–0.35. As can be seen in Figs. 7 and 8, it is characterized by a fast increase of water content at low relative pressure that corresponds to the completion of the first monolayer ($P/P_s \sim 0.25$) and a slower increase at higher relative pressure that corresponds to the formation of multiple layers of water molecules.

Microporosity induces an extremely steep increase of adsorbed water at very low relative pressure ($P/P_s < 0.05$) and a low relative pressure hysteresis. The phenomena are better visualized when relative pressure is plotted in a logarithmic scale. The hysteresis is due to water molecules strongly adsorbed in the micropores that remain stable for virtually infinite durations at low relative pressure unless temperature is increased. Thus, microporosity is a plausible hypothesis to explain the very low relative pressure part of the isotherms of JSC Mars-1 and ferrihydrite. The case of volcanic tuff is not so clear because the hysteresis between adsorption and desorption branches is quite small but the steep increase of water content at low RH (10^{-3}–10^{-2}) is well pronounced.

Delmelle et al. (2005) studied the water adsorption properties of six samples of fine volcanic ash particles and characterized their porosities. They found no detectable micropores but some of their samples showed a strong hysteresis persistent at very low relative humidity. The authors propose different hypotheses to explain this hysteresis. One is the hydroxylation of the surface of the mineral, supported by observations of characteristic near-IR absorption features. From our own spectral measurements, we do not see any evidence for hydroxylation in the case of the volcanic tuff, pure or mixed with Mg-sulfate.

Contrasting with all the other samples, in linear partial pressure scale, smectite SWy-2 presents a particular isotherm characterized by a convexity toward the pressure axis at high relative pressure. This shape classifies the SWy-2 smectite isotherm as an intermediate between the type II and type III isotherms (BDDT classification). The type III isotherm is characterized by a convexity toward the

pressure axis that is attributed to a cooperative process: "adsorption of the first water molecules promote the adsorption of further molecules" (Gregg and Sing, 1982). In the case of smectites, this behavior is well known and studied by a number of investigation methods (e.g. Rinnert, 2004; Salles, 2006). The solvation of the interlayer cations (mostly Na in the case of the SWy-2 smectite) induces swelling of the interlayer space, allowing for adsorption of larger quantities of water molecules in this particular site. In the case of Na-rich smectites like SWy-2, this swelling only occurs at relatively large relative humidity (RH > 0.1). This explains the intermediate place of this mineral isotherm between different classes as the particular convexity that defines the type III isotherm is only evident for large RH values. At lower RH, the isotherm is of type II, corresponding to adsorption on external particle surfaces. We do not see any convincing evidence for a developed microporosity in smectite SWy-2. There is a very limited but visible hysteresis that subsists at relative pressure of 10^{-3}. However, in the case of swelling phyllosilicates, low pressure hysteresis is more likely due to the consequences of swelling (not fully reversible change in the interlayer spacing) than to microporosity. Salles et al. (2008) studied the pore size distribution of a similar Na-rich smectite and classified all pores in this material as mesopores (>2 nm). The model of hydration for this smectite is also confirmed by the kinetics study (much more details will be provided in a separate article).

4.2. Results of the BET model

As seen in Fig. 9, the BET model (Brunauer et al., 1938) applies very successfully to all of our measurements in the 0.05–0.35 range of relative humidity. Results of linear fits are converted into values of specific surface area (m^2/kg) and BET adsorption parameter, *C*, reported in Table 3. Specific Surface Area (SSA) varies by a factor of 50 among our samples suite from the weakest (dunite) to the strongest (ferrihydrite) adsorbent. The value for JSC Mars-1 is close to the one for ferrihydrite, on the order of 10^5 m^2/kg. Value of SSA for smectite SWy-2 is a factor of two smaller (5×10^4 m^2/kg) while volcanic tuff, pure and mixed with Mg-sulfate, has a SSA value on the order of $\sim 10^4$ m^2/kg. Value for dunite is one order of magnitude lower ($\sim 10^3$ m^2/kg).

Values of SSA for montmorillonite obtained using the BET method are reported in the literature. Chevrier et al. (2008) report a value of 9×10^4 m^2/kg, close to the value we find for SWy-2 (5.4×10^4 m^2/kg). On the other hand, Zent and Quinn (1997) report a value of 6.6×10^5 m^2/kg which is more than ten times larger than our value for a very similar sample. A similar value (4.2×10^5 m^2/kg) was obtained by Mooney et al. (1952). Chevrier et al. (2008) made the hypothesis that the difference between their values and those measured previously comes from the use of a CO_2 atmosphere. However, even with no CO_2 in the chamber, we find a value close but significantly lower than the one reported by Chevrier et al. (2008). It is possible that the low value that we obtain is due to the use of larger particles (25–50 μm) than other investigators. However, another source of inconsistency between results obtained by different authors could come from the way the BET model is applied to smectite adsorption isotherm data. Smectites have the ability to swell as they adsorb water. Therefore, both their specific surface area and the *C* constants are modified during the hydration process. The BET model is usually applied over the range of relative humidity 0.05–0.35, which is the range of linearity in the classical BET plot. However, this may not be true for swelling phyllosilicates like smectites that present different ranges of linearity within this pressure range with different values of SSA and *C* parameters. Salles (2006) uses two different ranges of relative humidity: 0.05–0.10 and 0.10–0.25 to define two values of SSA and two values of *C* that, respectively, correspond to adsorption on external surfaces and adsorption in the interlayer space. Depending on the range of relative humidity used by different investigators to apply the BET model, these parameters could display a large dispersion.

Values of SSA are reported by Delmelle et al. (2005) for six different volcanic ash samples with various origins and compositions. They report values between 5×10^3 and 2×10^4 m^2/kg. Values of SSA also have been reported for fine basaltic powders by Zent and Quinn (1997) and Bryson et al. (2008), between 1.5 and 2.6×10^4 m^2/kg depending on particle size. These values are very close to the one we find for basaltic volcanic tuff (1.4×10^4 m^2/kg).

N_2 adsorption isotherms measured on ferrihydrite (Weidler, 1997) led to values between 2.7 and 3.1×10^5 m^2/kg depending on the sample preparation method. With H_2O, we find a value of the same order of magnitude but lower by about a factor of two.

Our six samples display a very large range of the adsorption constant, *C*, from 5 to 200, highlighting the large differences in the strength of water–mineral interactions. Delmelle et al. (2005) also reported values of the *C* parameter for their six volcanic ash samples. As this parameter is highly dependent on temperature, with the isotherms by Delmelle et al. (2005) being measured to 303 K, we convert their values at the temperature of our measurements (243 K) using equations from Brunauer et al. (1938). Calculated values of *C* range between 42 and 207 at 243 K, consistent with the value we measure for basaltic tuff (149). Bryson et al. (2008) report a value for *C* that, extrapolated to 243 K, is around 70 for basaltic powder. For Na-rich smectite, the *C* value measured by Salles (2006) and extrapolated to 243 K is around 4. For smectite SWy-2, we also find a very small value: 5.7. This low value of C is related to the particular shape of the isotherm for smectite, close to the type III shape ($C < 2$). Chevrier et al. (2008) measured a value of *C* that, extrapolated to 243 K, is 45. As already discussed before, both the relative pressure range on which the BET model is applied and the clay swelling properties related to its cationic composition are likely to influence the value of *C* and explain large differences between different measurements.

4.3. Spectral features of water in hydrated minerals

The diversity of the interactions between water and minerals already revealed by the quantification of ad(ab-)sorbed water, the shapes of the adsorption and desorption isotherms and the results of the BET treatment is confirmed by the analysis of the near-infrared reflectance spectra.

4.3.1. Comparison between different samples

For each of the six samples, we calculate the spectral ratio between the reflectance spectra of the sample in the most hydrated and the driest states (Fig. 16). These ratios represent the absorption due to the totality of the water trapped into the samples after all the successive sorption steps. It is then possible to study the spectral features of water independently from other spectral features not related to water. As the variation of water content between the most hydrated and driest states is very different for each sample (see Table 1), we have chosen to normalize all the ratios at one wavelength in the continuum (at 2.3 μm) and at a second wavelength in the region of the maximum of the absorption (at 3.02 μm). By this way, we scale the spectral ratio to get the same continuum and the same contrast in the most intense absorption band, facilitating the qualitative comparison of spectral features between the different samples.

For comparison, we also plot $-\ln(k)$ for liquid water and crystalline ice, where *k* is the imaginary part of the water optical constants. Optical constants from the near-infrared to the far infrared are determined for crystalline water ice at 145 K by Grundy and Schmitt (1998) and Schmitt et al. (1998). Optical constants for

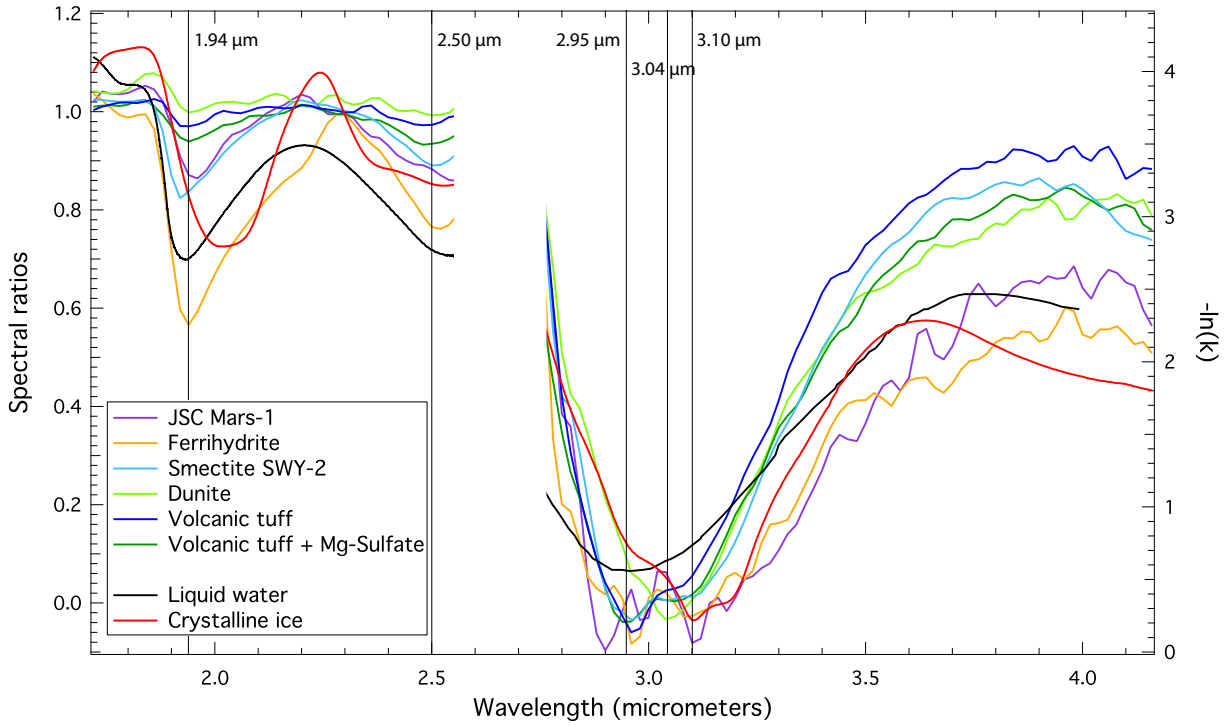

Fig. 16. Normalized spectral ratios (left scale) between the most hydrated and driest states (from Figs. 10–15) for each of the six samples. These ratios are compared with the absorption coefficients of liquid water and crystalline ice (right scale). Spectral ratios are cut between 2.55 and 2.75 µm to hide unreliable values due to variations of the absorption by water vapor in the room (between the chamber and the detector) during measurements.

liquid water are determined by Grundy and Schmitt (1998) from the visible up to 2.5 µm and by Segelstein (1981) at longer wavelengths. The spectral features of adsorbed water for the six samples closely match those of liquid water. Even the very narrow absorption around 1.8 µm that is clearly visible on liquid water optical constants appears for the most hydrated samples: the palagonite JSC Mars-1 and ferrihydrite.

However, comparison between spectral ratios for the six samples and optical constants of liquid water also highlight differences both in the 1.9 and 3-µm bands. Both the positions of the absorption maxima and the shapes of the bands show a pronounced variability. These spectral differences are not directly linked to differences in water content between the samples (see Table 2). For all the samples, we note a more or less pronounced asymmetry: absorption is wider in the longer wavelength side of the band, which appears to be a common behavior for all hydration water bands (Bishop et al., 1994). This is also observed for liquid water whereas an asymmetry in the opposite way is observed for crystalline water ice. The integrated intensity and depth of the 1.9-µm band (normalized to the absorption at 3 µm) for ferrihydrite are considerably increased compared to all other samples and the position of the maximum of reflectance after the band is found at a far longer wavelength for ferrihydrite (2.3 µm) than for all other samples and liquid water (2.2 µm). This last observation could be explained by some addition of structural OH^- during the hydration sequence that would be responsible for the narrow absorption around 2.2 µm visible as a shoulder on the broad 1.9-µm band. Observation of a stronger absorption at 2.7 µm on the same spectral ratio (not shown) is further evidence for such a hydroxylation. In the case of the JSC Mars-1 palagonite, a shoulder is also present at 2.05 µm on the long-wavelength wing of the 1.9-µm band.

The spectral region between 2.2 and 2.5 µm is interesting for various reasons. Absorption in this region is usually interpreted as the short wavelength wing of the strong 3-µm absorption band. However, a minimum of reflectance can be defined around 2.5 µm for all of our samples except JSC Mars-1. No maximum of the broad absorption around 2.5 µm is visible in liquid water optical constants. However, a wide absorption band at about 2.52 µm is documented in the spectrum of crystalline water ice (Grundy and Schmitt, 1998).

Variability of spectral features among our sample suite is also evident for the broad 3-µm band. Unfortunately, the region of the maximum of absorption in the 3-µm band cannot be studied using spectral ratios for the JSC Mars-1 and ferrihydrite samples because of a low signal-to-noise ratio due to the small values of reflectance. The volcanic tuff, pure or mixed with Mg-sulfate and the smectite SWy-2 present very similar spectral features with two maxima of absorption, at approximately 2.96 and 3.06 µm. On the contrary, the spectral ratio for dunite only shows one maximum of absorption at 3.04 µm. All these four samples differ from the case of liquid water that presents one maximum of absorption at 2.96 µm. Spectral variability is also evident in the long-wavelength wing of the 3-µm band both among the samples suite and in comparison with liquid and crystalline water.

4.4. Comparison between different steps of the adsorption isotherms

While we previously compared the average spectral features of the total amount of water adsorbed on each sample, it is also possible to look at continuous variations of spectral features of water during the hydration process. Calculation of absorption band barycenters is a convenient way to examine variations of bands position and shape during hydration. Fig. 17 presents the evolutions of the position of the 3-µm band barycenter as a function of its intensity (band area). Fig. 18 presents the same evolutions for the 1.9-µm band. These evolutions are only plotted for the three most adsorbing samples as this band is too weak in other samples to obtain a satisfactory signal-to-noise ratio. Both Figs. 17 and 18 demonstrate the evolution of the spectral features of water during sample hydration. In these barycenter position/band intensity diagrams, clear trends for the 3-µm

band are observed for all samples except Mg-sulfate/tuff mixture. For palagonite JSC Mars-1, ferrihydrite, dunite and pure volcanic tuff, barycenter of the 3-μm band shifts to longer wavelength as water adsorbs. Smectite presents a S-shaped trend representative of the different processes corresponding to different steps of hydration during the swelling process. The position of the 1.9 μm band barycenter (Fig. 18) shifts to longer wavelength during the hydration process for the palagonite JSC Mars-1 and smectite SWy-2. On the contrary, in the case of ferrihydrite, the barycenter of this band shifts to shorter wavelength. This behavior is chiefly due to the initial position of the 1.9-μm band barycenter situated at very long wavelength for this sample.

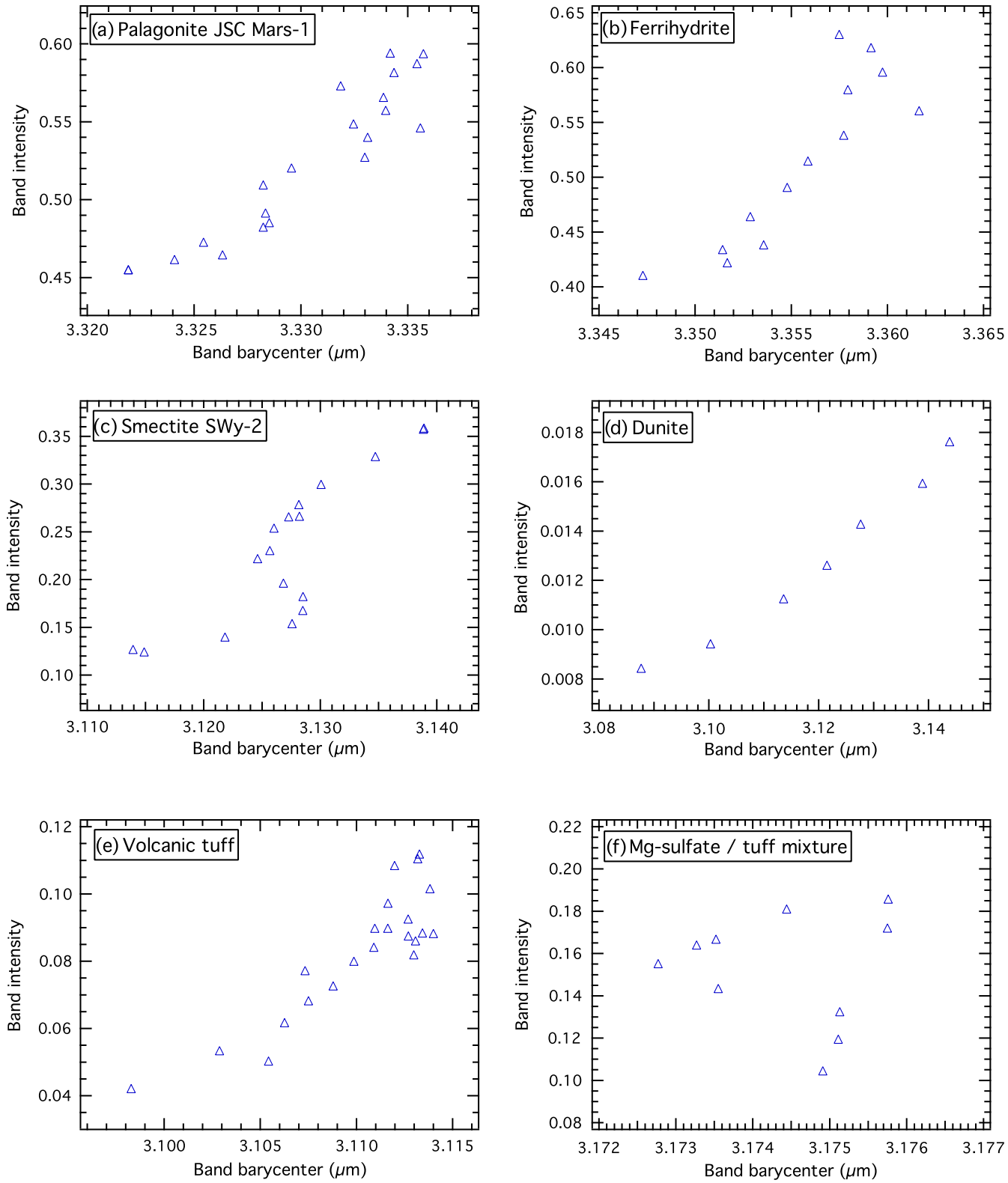

Fig. 17. Evolution of the position of the 3-μm band barycenter as a function of its intensity during the hydration process for the six samples. Increase of band intensity (from bottom to top on the vertical axis) indicates an increase of the amount of adsorbed water.

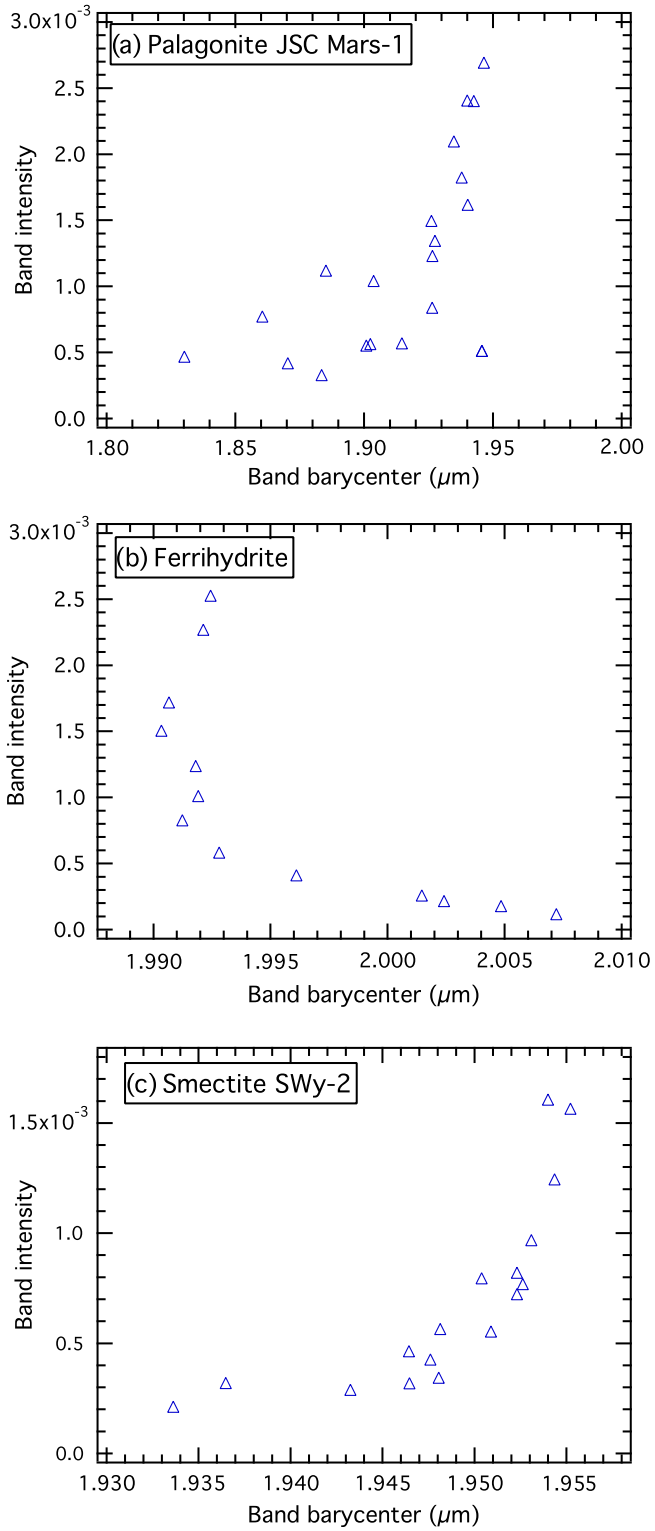

Fig. 18. Evolution of the position of the 1.9-μm band barycenter as a function of its intensity during the hydration process for palagonite "JSC Mars-1", ferrihydrite and smectite SWy-2. Increase of band intensity (from bottom to top on the vertical axis) indicates an increase of the amount of adsorbed water.

Such evolutions of band positions and shapes during adsorption and/or desorption processes are also reported by other authors for different samples: Bishop et al. (1994) for montmorillonite SWy exchanged with different cations, Rinnert (2004) for montmorillonite and Richard et al. (2006) for silica and magnesium oxide.

4.5. Comparison between structural and adsorbed water in the case of Mg-sulfate

It is interesting to compare all the previous spectral ratios with the case of Mg-sulfate for which we can independently derive the spectral signatures of both structural and adsorbed water. The spectral signature of structural water is derived by normalizing the spectrum of epsomite ($MgSO_4 \cdot 7H_2O$) mixed with volcanic tuff by the spectrum of kieserite ($MgSO_4 \cdot H_2O$), also mixed with volcanic tuff in the same proportion, obtained by dehydration of the initial epsomite/kieserite mixture heated at 170 °C under high vacuum. The spectral signature of adsorbed water is obtained as explained before for all the other samples. Both spectral ratios are plotted in Fig. 19. Differences between the spectral ratios of the two types of hydration water are very important but their quantitative comparison is not straightforward due to the very different amount of water involved in each case. However, the obvious differences in both the 1.9 and 3-μm band shapes cannot be attributed to an effect of the different amounts of water. The maximum of the 1.9-μm absorption is located at shorter wavelength in the case of adsorbed water. For the 3-μm band, the shape of the absorption feature is clearly different, especially at the longest wavelengths where the position of the maximum of reflectance after the band is found, respectively, at 3.95 and 3.75 μm for adsorbed and structural water.

Comparison with optical constants of liquid water and crystalline ice is particularly instructive. However, it must also be kept in mind that water absorption band positions are affected not only by whether the water is in liquid or solid form, but also by how the water molecules are configured relative to nearest neighbor cations and what those cations are.

In the spectral range: 1.25–2.5 μm, the spectral features of structural water in epsomite closely match those of crystalline ice. The most interesting feature in this spectral range is the weak absorption band at 1.65 μm. Grundy and Schmitt (1998) studied this particular band in crystalline ice. As its position and strength are particularly dependent on temperature in water ice, this band can be used as a very accurate thermometer. It could be interesting to check if this behavior is also valid for this band in epsomite and could define a thermometer for this mineral. The main differences between epsomite structural water and crystalline ice are the position of the 1.9-μm band found at lower wavelength in epsomite structural water and the shape of the absorption between 2.3 and 2.5 μm with a break of slope at 2.36 μm in the case of crystalline ice that is not visible for structural water. In the case of adsorbed water, the position of its 1.9-μm band is coherent with liquid water but a different behavior occurs in the 2.8–4.2 μm spectral range. In the region of the maximum of absorption around 3.0 μm, structural and adsorbed waters show very similar shapes with two absorptions around 2.95 and 3.10 μm whereas liquid water presents only one wide absorption at 2.96 μm. Crystalline ice has its maximum of absorption at 3.10 μm but also one shoulder on the low wavelength wing at 2.96 μm and another one on the high wavelength wing at 3.20 μm. Finally, the position of the maximum of reflectance after the band is consistent with liquid water in the case of structural water and with neither liquid water nor crystalline ice in the case of adsorbed water.

5. Conclusion

We have characterized the sorption of water onto martian soil analog samples using thermodynamics and near-infrared reflectance spectroscopy. The results of this study are the adsorption and desorption isotherms and the corresponding series of reflectance spectra for six materials: palagonite JSC Mars-1, ferrihydrite,

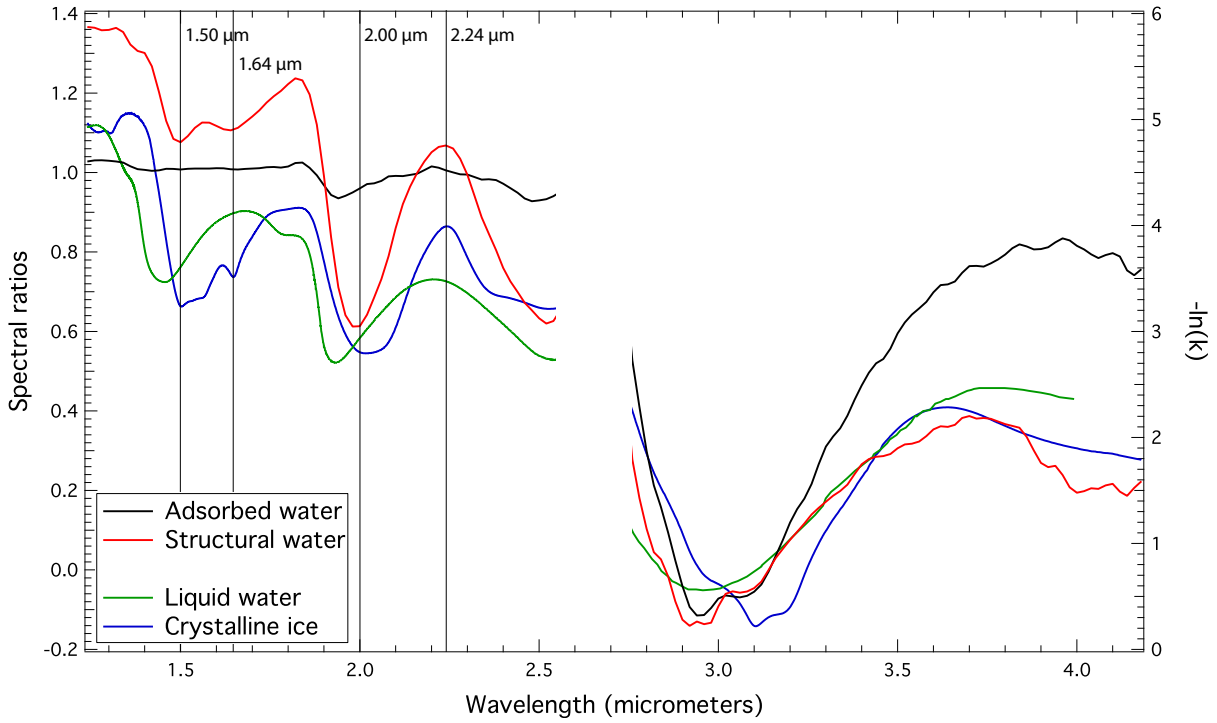

Fig. 19. Spectral ratios (left scale) calculated from the Mg-sulfate/volcanic tuff mixture spectra corresponding to structural and adsorbed water. These ratios are compared with the absorption coefficients of liquid water and crystalline ice (right scale). Spectral ratios are cut between 2.55 and 2.75 µm to hide unreliable values due to variations of the absorption by water vapor in the room (between the chamber and the detector) during measurements.

smectite SWy-2, dunite, basaltic tuff and Mg-sulfate/basaltic tuff mixture. Measurements were made at −30 °C in the range of relative humidity: 10^{-4}–0.70. A BET treatment of the adsorption isotherms reveals variations of the specific surface areas among samples over two orders of magnitude between an unaltered mafic material (dunite, olivine and pyroxenes) and the palagonitic soil JSC Mars-1 and nanophase oxide ferrihydrite (respectively, 10^3 and 10^5 m^2/kg). Using one of these values instead of another in a martian model of interaction between atmosphere and regolith will have severe consequences on the fluxes of water between these reservoirs. Smectite clays and basalt are very popular materials used in a number of studies considering the role of the regolith in the martian global water cycle. However, we emphasize that nanophase iron oxides like ferrihydrite and magnetite contained in the JSC Mars-1 palagonitic soil have extremely large specific surface areas as a result of their small particle size and are particularly widespread on Mars. If their concentrations are shown to be significant, we think that the properties of these materials should be considered in the regolith/atmosphere interaction models. Very strong contrasts of adsorption properties should also occur in areas covered by fine wind-deposited dust and mafic crust. We especially note that the global repartitions of nanophase ferric oxide on the surface (Poulet et al., 2007), hydrogen in the subsurface (Feldman et al., 2004) and annually averaged water vapor in the atmosphere (Jakosky et al., 2005) present similar spatial patterns that may indicated a link between these different water reservoirs.

Among our samples, a large variability in the type of interaction between water and minerals is revealed by the shape of the adsorption and desorption isotherms. Depending on the sample and the range of relative humidity, the sorption properties can be dominated by adsorption on external surfaces, in micropores, in phyllosilicates interlayer sites and even eventually bounded water and/or hydroxyl ions. The modalities of water exchange between atmosphere and regolith on Mars will be strongly affected by the nature of the interaction between the water molecules and the mineral. For example, a strong hysteresis at very low relative humidity associated with microporosity could be responsible for a large amount of water retained in the regolith even under very dry conditions and then a limitation of exchange with atmosphere. The presence or absence of materials presenting cooperative effects during adsorption of water like swelling phyllosilicates will also have a strong impact on the exchanges.

The near-infrared reflectance spectra acquired during the adsorption and desorption sequences reveal the strong variations of the absorption band attributed to water over the range of relative humidity expected on Mars. Using these spectra, we can characterize the spectral features of sorbed water for the different materials as well as water sorbed at different values of relative pressure. These ratios reveal differences in the spectral features that are documented and compared to previous studies. This documentation should be useful to interpret remote-sensing datasets of the martian surface or the surfaces of other Solar System objects where hydrated minerals are present. Contrasted spectral signatures of structural water and water adsorbed in different sites of the mineral could especially be used to decipher the physical state of water of hydration on these surfaces by near-infrared remote sensing.

Acknowledgments

This work has been supported by the French « Programme National de Planétologie » from CNRS and by the « Centre National d'Etudes Spatiales ». We acknowledge Vincent Chevrier and Edouard Cloutis for constructive reviews that improved the quality of this paper in a very significant manner.

References

Allen, C.C., Morris, R.V., Lindstrom, D.J., Lindstrom, M.M., Lockwood, J.P., 1997. JSC Mars-1 – Martian regolith simulant. LPSC XXVIII (abstract 1797).

Allen, C.C., Morris, R.V., Jager, K.M., Golden, D.C., Lindstrom, D.J., Lindstrom, M.M., Lockwood, J.P., 1998. Martian regolith simulant JSC Mars-1. LPSC XXIX (abstract 1690).

Anderson, D.M., Schwarz, M.J., Tice, A.R., 1978. Water vapor adsorption by sodium montmorillonite at −5 °C. Icarus 34, 638–644.

Bandfield, J.L., 2002. Global mineral distributions on Mars. J. Geophys. Res. 107. doi:10.1029/2001JE001510.

Bibring, J.-P., Langevin, Y., Soufflot, A., Combes, M., Cara, C., 1989. Results from the ISM experiment. Nature 341, 591–593.

Bibring, J.-P., Langevin, Y., Mustard, J.F., Poulet, F., Arvidson, R., Gendrin, A., Gondet, B., Mangold, N., Pinet, P., Forget, F., 2006. Global mineralogical and aqueous Mars history derived from OMEGA/Mars express data. Science 312, 400–404.

Bish, D.L., Carey, J.W., Vaniman, D.T., Chipera, S.J., 2003. Stability of hydrous minerals on the martian surface. Icarus 164, 96–103.

Bishop, J.L., Pieters, C.M., 1995. Low-temperature and low atmospheric pressure infrared reflectance spectroscopy of Mars soil analog materials. J. Geophys. Res. 100, 5369–5379.

Bishop, J.L., Pieters, C.M., Burns, R.G., 1993. Reflectance and Moessbauer spectroscopy of ferrihydrite-montmorillonite assemblages as Mars soil analog materials. Geochim. Cosmochim. Acta 57, 4583–4595.

Bishop, J.L., Pieters, C.M., Edwards, J.O., 1994. Infrared spectroscopic analyses on the nature of water in montmorillonite. Clays Clay Miner. 42, 702–716.

Bishop, J.L., and 11 colleagues, 2008. Phyllosilicate diversity and past aqueous activity revealed at Mawrth Vallis, Mars. Science 321, 830–833.

Bonello, G., Berthet, P., D'Hendecourt, L., 2005. Identification of magnesium sulfate hydration state derived from NIR reflectance spectroscopy. LPSC XXXVI (abstract 1996).

Bonnefoy, N., 2001. Développement d'un spectro-goniomètre pour l'étude de la réflectance bidirectionnel le des surfaces géophysiques. Application au soufre et perspectives pour le satellite Io. PhD thesis, Université Joseph Fourier, Grenoble.

Boynton, W.V., and 24 colleagues, 2002. Distribution of hydrogen in the near surface of Mars: Evidence for subsurface ice deposits. Science 297, 81–85.

Brissaud, O., Schmitt, B., Bonnefoy, N., Douté, S., Rabou, P., Grundy, W., Fily, M., 2004. Spectrogonio radiometer for the study of the bidirectional reflectance and polarization functions of planetary surfaces. 1. Design and tests. Appl. Opt. 43, 1926–1937.

Brunauer, S., Emmet, P.H., Teller, E., 1938. Adsorption of gases in multimolecular layers. J. Am. Chem. Soc. 90, 309–319.

Brunauer, S., Deming, L.S., Deming, W.S., Teller, E., 1940. On a theory of the van der Waals adsorption of gases. J. Am. Chem. Soc. 62, 1723–1732.

Bryson, K.L., Chevrier, V., Sears, D.W.G., Ulrich, R., 2008. Stability of ice on Mars and the water vapor diurnal cycle: Experimental study of the sublimation of ice through a fine-grained basaltic regolith. Icarus 196, 446–458.

Burnett, M.G., Galway, A.K., Lawther, C., 1996. Ideality of water vapour and its adsorption on the glass surfaces of a conventional glass vacuum apparatus at 295 K between 0 and 10 Torr. J. Chem. Soc., Faraday Trans. 92, 4301–4304.

Campbell, J.L., Gellert, R., Lee, M., Mallett, C.L., Maxwell, J.A., O'Meara, J.M., 2008. Quantitative in situ determination of hydration of bright high-sulfate martian soils. J. Geophys. Res.. doi:10.1029/2007JE002959.

Chevrier, V.D., Sears, W.G., Chittenden, J.D., Roe, L.A., Ulrich, R., Bryson, K., Billingsley, L., Hanley, J., 2007. Sublimation rate of ice under simulated Mars conditions and the effect of layers of mock regolith JSC Mars-1. Geophys. Res. Lett. 34. doi:10.1029/2006GL028401.

Chevrier, V., Ostrowski, D.R., Sears, D.W.G., 2008. Experimental study of the sublimation of ice through an unconsolidated clay layer: Implications for the stability of ice on Mars and the possible diurnal variations in atmospheric water. Icarus 196, 459–476.

Chipera, S.J., Vaniman, D.T., 2007. Experimental stability of magnesium sulfate hydrates that may be present on Mars. Geochim. Cosmochim. Acta 71, 241–250.

Chou, I.-M., Seal, R.R., 2007. Magnesium and calcium sulfate stabilities and the water budget of Mars. J. Geophys. Res. 112. doi:10.1029/2007JE002898.

Cloutis, E.A., Craig, M.A. Mustard, J.F., Kruzelecky, R.V., Jamroz, W.R., Scott, A., Bish, D.L., Poulet, F., Bibring, J.-P., King, P.L., 2007. Stability of hydrated minerals on Mars. Geophys. Res. Lett. 34, L20202.

Cloutis, E.A., Craig, M.A., Kruzelecky, R.V., Jamroz, W.R., Scott, A., Hawthorne, F.C., Mertzman, S.A., 2008. Spectral reflectance properties of minerals exposed to simulated Mars surface conditions. Icarus 195, 140–168.

Costanzo, P.M., Guggenheim, S., 2001. Baseline studies of the clay minerals society source clays: Preface. Clays Clay Miner. 49, 371.

Delmelle, P., Villieras, F., Pelletier, M., 2005. Surface area, porosity and water adsorption properties of fine volcanic ash particles. Bull. Volcanol. 67, 160–169.

Dontsova, K.M., Norton, L.D., Johnston, C.T., Bigham, J.M., 2004. Influence of exchangeable cations on water adsorption by soil clays. Soil Sci. Soc. Am. J. 68, 1218–1227.

Fanale, F.P., Cannon, W.A., 1971. Adsorption on the martian regolith. Nature 230, 502–504.

Farrand, W.H., and 13 colleagues, 2007. Visible and near-infrared multispectral analysis of rocks at Meridiani Planum, Mars, by the Mars Exploration Rover Opportunity. J. Geophys. Res. 112. doi: 10.1029/2006JE002773.

Feldman, W.C., and 12 colleagues, 2002. Global distribution of neutrons from Mars: Results from Mars Odyssey. Science 297, 75–78.

Feldman, W.C., and 14 colleagues, 2004. Global distribution of near-surface hydrogen on Mars. J. Geophys. Res. 109. doi: 10.1029/2003JE002160.

Feldman, W.C., Bandfield, J.L., Diez, B., Elphic, R.C., Maurice, S., Nelli, S.M., 2008. North to south asymmetries in the water-equivalent hydrogen distribution at high latitudes on Mars. J. Geophys. Res. 113. doi:10.1029/2007JE003020.

Frinak, E.K., Mashburn, C.D., Tolbert, M.A., Toon, O.B., 2005. Infrared characterization of water uptake by low-temperature Na-montmorillonite: Implications for Earth and Mars. J. Geophys. Res. 110. doi:10.1029/2004JD005647.

Gendrin, A., and 10 colleagues, 2005. Sulfates in martian layered terrains: The OMEGA/Mars Express view. Science 307, 1587–1591.

Gregg, S.J., Sing, K.S.W., 1982. Adsorption, Surface Area and Porosity. Academic Press, 303 p.

Grundy, W.M., Schmitt, B., 1998. The temperature-dependent near-infrared absorption spectrum of hexagonal H_2O ice. J. Geophys. Res. 103, 25809–25822.

Hapke, B., 1993. Theory of Reflectance and Emittance Spectroscopy. Topics in Remote Sensing. Cambridge University Press, Cambridge, UK, 455 p.

Hensen, E.J.M., Tambach, T.J., Bliek, A., Smit, B., 2001. Adsorption isotherms of water in Li-, Na-, and K-montmorillonite by molecular simulation. J. Chem. Phys. 115, 3322–3329.

Holt, J.W.and 11 colleagues, 2008. Radar sounding evidence for buried glaciers in the southern mid-latitudes of Mars. Science 322, 1235–1238.

Hudson, T.L., Aharonson, O., Schorghofer, N., Farmer, C.B., Hecht, M.H., Bridges, N.T., 2007. Water vapor diffusion in Mars subsurface environments. J. Geophys. Res. 112. doi:10.1029/2006JE002815.

Hunt, G.R., Logan, L.M., Salisbury, J.W., 1973. Mars: Components of infrared spectra and the composition of the dust cloud. Icarus 18, 459–469.

Jakosky, B.M., Mellon, M.T., Varnes, E.S., Feldman, W.C., Boynton, W.V., Haberle, R.M., 2005. Mars low-latitude neutron distribution: Possible remnant near-surface water ice and a mechanism for its recent emplacement. Icarus 175, 58–67.

Jänchen, J., Bish, D.L., Möhlmann, D.T.F., Stach, H., 2006. Investigation of the water sorption properties of Mars-relevant micro- and mesoporous minerals. Icarus 180, 353–358.

Jänchen, J., Morris, R.V., Bish, D.L., Janssen, M., Hellwig, U., 2009. The H_2O and CO_2 adsorption properties of phyllosilicate-poor palagonitic dust and smectites under martian environmental conditions. Icarus 200, 463–467.

Jouglet, D., Poulet, F., Milliken, R.E., Mustard, J.F., Bibring, J.-P., Langevin, Y., Gondet, B., Gomez, C., 2007. Hydration state of the martian surface as seen by Mars Express OMEGA: 1. Analysis of the 3 μm hydration feature. J. Geophys. Res. 112. doi:10.1029/2006JE002846.

Kuzmin, R.O., Zabalueva, E.V., Mitrofanov, I.G., Litvak, M.L., Rodin, A.V., Boynton, W.V., Saunders, R.S., 2007. Seasonal redistribution of water in the superficial martian regolith: Results from the Mars Odyssey High-Energy Neutron Detector (HEND). Solar Syst. Res. 41, 89–102.

Likos, W.J., Lu, N., 2001. Water adsorption characteristics of smectite/kaolinite clay mixtures for engineered waste Barriers. In: Eleventh Annual V. M. Goldschmidt Conference (abstract 3057).

Manceau, A., Gates, W.P., 1997. Surface structural model for ferrihydrite. Clays Clay Miner. 45, 448–460.

Michel, F.M., Ehm, L., Antao, S.M., Lee, P.L., Chupas, P.J., Liu, G., Strongin, D.R., Schoonen, M.A.A., Phillips, B.L., Parise, J.B., 2007a. The structure of ferrihydrite, a nanocrystalline material. Science 316, 1726–1729.

Michel, F.M., and 15 colleagues, 2007. Similarities in 2- and 6-line ferrihydrite based on pair distribution function analysis of X-ray total scattering. Chem. Mater. 19(6), 1489–1496.

Milliken, R.E., Mustard, J.F., 2005. Quantifying absolute water content of minerals using near-infrared reflectance spectroscopy. J. Geophys. Res. 110. doi:10.1029/2005JE002534.

Milliken, R.E., Mustard, J.F., 2007a. Estimating the water content of hydrated minerals using reflectance spectroscopy. I. Effects of darkening agents and low-albedo materials. Icarus 189, 550–573.

Milliken, R.E., Mustard, J.F., 2007b. Estimating the water content of hydrated minerals using reflectance spectroscopy. II. Effects of particle size. Icarus 189, 574–588.

Milliken, R.E., Mustard, J.F., Poulet, F., Jouglet, D., Bibring, J.-P., Gondet, B., Langevin, Y., 2007. Hydration state of the martian surface as seen by Mars Express OMEGA: 2. H_2O content of the surface. J. Geophys. Res. 112. doi:10.1029/2006JE002853.

Mitrofanov, I., and 11 colleagues, 2002. Maps of subsurface hydrogen from the High Energy Neutron Detector, Mars Odyssey. Science 297, 78–81.

Mooney, R.W., Keenan, A.G., Wood, L.A., 1952. Adsorption of water vapor by montmorillonite. I. Heat of desorption and application of BET theory. J. Am. Chem. Soc. 74, 1367–1371.

Mustard, J.F., and 35 colleagues, 2008. Hydrated silicate minerals on Mars observed by the Mars Reconnaissance Orbiter CRISM instrument. Nature 454, 305–309.

Peterson, R.C., Wang, R., 2006. Crystal molds on Mars: Melting of a possible new mineral species to create martian chaotic terrain. Geology 34, 957–960.

Plaut, J.J., Safaeinili, A., Holt, J.W., Phillips, R.J., Campbell, B.A., Carter, L.M., Leuschen, C., Gim, Y., Seu, R., Sharad Team, 2008. Radar evidence for ice in Lobate Debris Aprons in the mid-northern latitudes of Mars. LPSC XXXIX (abstract 2290).

Pommerol, A., Schmitt, B., 2008a. Strength of the H_2O near-infrared absorption bands in hydrated minerals: Effects of particle size and correlation with albedo. J. Geophys. Res. 113. doi:10.1029/2007JE003069.

Pommerol, A., Schmitt, B., 2008b. Strength of the H_2O near-infrared absorption bands in hydrated minerals: Effects of measurement geometry. J. Geophys. Res. 113. doi:10.1029/2008JE003197.

Poulet, F., Bibring, J.-P., Mustard, J.F., Gendrin, A., Mangold, N., Langevin, Y., Arvidson, R.E., Gondet, B., Gomez, C., 2005. Phyllosilicates on Mars and implications for early martian climate. Nature 438, 623–627.

Poulet, F., Gomez, C., Bibring, J.-P., Langevin, Y., Gondet, B., Pinet, P., Belluci, G., Mustard, J., 2007. Martian surface mineralogy from Observatoire pour la Minéralogie, l'Eau, les Glaces et l'Activité on board the Mars Express spacecraft (OMEGA/MEx): Global mineral maps. J. Geophys. Res. 112. doi:10.1029/2006JE002840.

Prieto-Ballesteros, O., Fernandez-Remolar, D., Mateo-Martí, E., Fernandez-Sampedro, M., Kargel, J.S., Friedlander, L.R., Martín-Gago, J.A., 2007. Phase stability experiments of hydrated magnesium sulfates at environmental conditions of martian surface. LPSC XXXVIII 38 (abstract 1512).

Putzig, N.E., Mellon, M.T., 2007. Apparent thermal inertia and the surface heterogeneity of Mars. Icarus 191, 68–94.

Richard, T., Mercury, L., Poulet, F., d'Hendecourt, L., 2006. Diffuse reflectance infrared Fourier transform spectroscopy as a tool to characterise water in adsorption/confinement situations. J. Colloid Interf. Sci. 304, 125–136.

Rinnert, E., 2004. Etats d'hydratation d'argiles suivis par analyses vibrationnel les de l'eau et des hydroxyles dans le proche infrarouge: Application aux systèmes saponite et bentonite. PhD thesis, Université Henri Poincaré, Nancy I.

Salles, F., 2006. Séquence d'hydratation multi-échel le. Détermination des énergies macroscopiques à partir des propriétés microscopiques. PhD thesis, Université Paris VI – Pierre et Marie Curie.

Salles, F., Beurroies, I., Bildstein, O., Jullien, M., Raynal, J., Denoyel, R., Damme, H.V., 2008. A calorimetric study of mesoscopic swelling and hydration sequence in solid na-montmorillonite. Appl. Clay Sci. 39, 186–201.

Schmitt, B., Quirico, E., Trotta, F., Grundy, W.M., 1998. Optical Properties of Ices from UV to Infrared, in Solar System Ices. Astrophysics Space Science Library, vol. 227. Kluwer Academic, Norwell, Mass. pp. 199–240.

Schorghofer, N., 2007. Dynamics of ice ages on Mars. Nature 449, 192–194.

Schorghofer, N., Aharonson, O., 2005. Stability and exchange of subsurface ice on Mars. J. Geophys. Res. 110. doi:10.1029/2004JE002350.

Segelstein, D., 1981. The complex refractive index of water. Master's thesis, Univ. of Mo. at Kansas City.

Squyres, S.W., and 18 colleagues, 2004. In situ evidence for an ancient aqueous environment at Meridiani Planum, Mars. Science 306, 1709–1714.

Treiman, A.H., Barrett, R.A., Gooding, J.L., 1993. Preterrestrial aqueous alteration of the Lafayette (SNC) meteorite. Meteoritics 28, 86–97.

Vaniman, D.T., Bish, D.L., Chipera, S.J., Fialips, C.I., William Carey, J., Feldman, W.C., 2004. Magnesium sulphate salts and the history of water on Mars. Nature 431, 663–665.

Wagner, W., Pruss, A., 2002. The IAPWS Formulation 1995 for the thermodynamic properties of ordinary water substance for general and scientific use. J. Phys. Chem. Ref. Data 31, 387–535.

Wang, A., Freeman, J.J., Jolliff, B.L., Chou, I.-M., 2006a. Sulfates on Mars: A systematic Raman spectroscopic study of hydration states of magnesium sulfates. Geochim. Cosmochim. Acta 70, 6118–6135.

Wang, A., and 12 collegues, 2006b. Sulfate deposition in subsurface regolith in Gusev crater, Mars. J. Geophys. Res. 111. doi: 10.1029/2005JE002513.

Weidler, P.G., 1997. BET sample pretreatment of synthetic ferrihydrite and its influence on the determination of surface area and porosity. J. Porous Mater. 4, 165–169.

Wray, J.J., Ehlmann, B.L., Squyres, S.W., Mustard, J.F., Kirk, R.L., 2008. Compositional stratigraphy of clay-bearing layered deposits at Mawrth Vallis, Mars. Geophys. Res. Lett. 35. doi:10.1029/2008GL034385.

Zent, A.P., Quinn, R.C., 1997. Measurement of H_2O adsorption under Mars-like conditions: Effects of adsorbent heterogeneity. J. Geophys. Res. 102, 9085–9096. doi:10.1029/96JE03420.

Zent, A.P., Haberle, R.M., Houben, H.C., Jakosky, B.M., 1993. A coupled subsurface-boundary layer model of water on Mars. J. Geophys. Res. 98, 3319–3337.

Zent, A.P., Howard, D.J., Quinn, R.C., 2001. H_2O adsorption on smectites: Application to the diurnal variation of H_2O in the martian atmosphere. J. Geophys. Res. 106, 14667–14674.